





EX LIBRIS
UNIVERSITATIS
ALBERTENSIS

The Bruce Peel
Special Collections
Library

University of Alberta

Library Release Form

Name of Author: Hendrick A. Sikkema

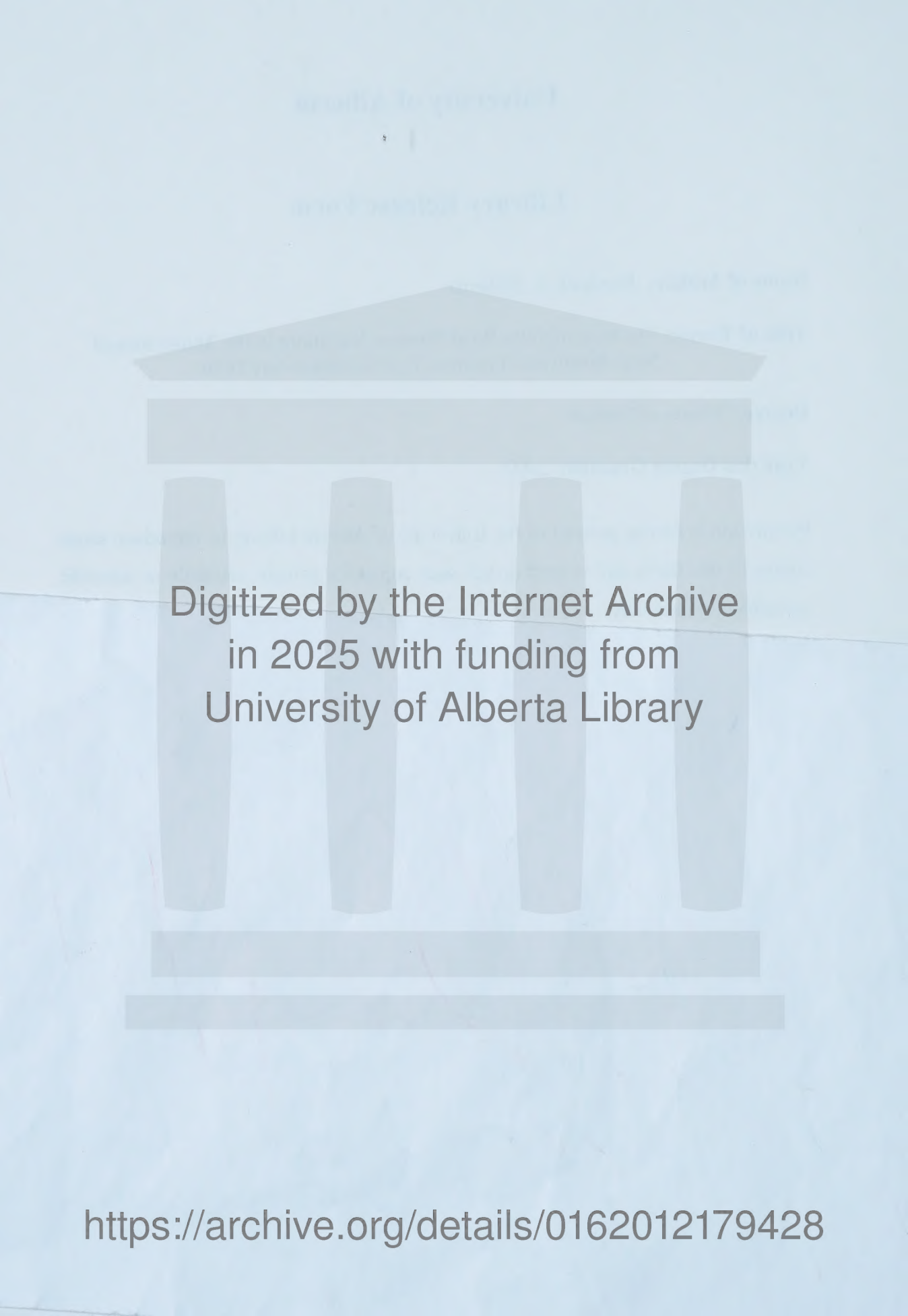
Title of Thesis: The Role of Solar Wind Pressure Variations in the Appearance of Near-Relativistic Electrons Near Geostationary Orbit

Degree: Master of Science

Year this Degree Granted: 2000

Permission is hereby granted to the University of Alberta Library to reproduce single copies of this thesis and to lend or sell such copies for private, scholarly or scientific research purposes only.

The author reserves all other publication and other rights in association with the copyright in the thesis, and except as hereinbefore provided, neither the thesis nor any substantial portion thereof may be printed or otherwise reproduced in any material form whatever without the author's prior written permission.



Digitized by the Internet Archive
in 2025 with funding from
University of Alberta Library

<https://archive.org/details/0162012179428>

Psalm 8

[KJV]

To the chief Musician upon Gittith, A Psalm of David

¹O LORD our Lord, how excellent is thy name in all the earth! who hast set thy glory above the heavens. ²Out of the mouth of babes and sucklings hast thou ordained strength because of thine enemies, that thou mightest still the enemy and the avenger.

³When I consider thy heavens, the work of thy fingers, the moon and the stars, which thou hast ordained; ⁴What is man, that thou art mindful of him? and the son of man, that thou visitest him? ⁵For thou hast made him a little lower than the angels, and hast crowned him with glory and honour. ⁶Thou madest him to have dominion over the works of thy hands; thou hast put all *things* under his feet: ⁷All sheep and oxen, yea, and the beasts of the field; ⁸The fowl of the air, and the fish of the sea, *and whatsoever* passeth through the paths of the seas. ⁹O LORD our Lord, how excellent is thy name in all the Earth!

University of Alberta

**The Role of Solar Wind Pressure Variations
in the Appearance of Near-Relativistic Electrons
Near Geostationary Orbit**

by

Hendrick A. Sikkema



A thesis submitted to the Faculty of Graduate Studies and Research
in partial fulfillment of the requirements for the degree of

Master of Science

Department of Physics

Edmonton, Alberta

Fall 2000

University of Alberta

Faculty of Graduate Studies and Research

The undersigned certify that they have read, and recommend to the Faculty of Graduate Studies and Research for acceptance, a thesis entitled "The Role of Solar Wind Pressure Variations in the Appearance of Near-Relativistic Electrons Near Geostationary Orbit" submitted by Hendrick A. Sikkema in partial fulfillment of the requirements for the degree of Master of Science.

Dedication

to the LORD God, Creator of the Universe
and Upholder of all things, now and forever.

Abstract

The objective of this thesis is to determine whether solar wind pressure variations may play a role in the energization of electrons to near-relativistic energies near geostationary orbit. The appearance of large amplitude ultra-low frequency (ULF) magnetic pulsations detected by ground based magnetometers just prior to rises in energetic electron fluxes suggests that, either the pulsations themselves energize the electrons or the source of energy for these pulsations rapidly accelerates the electrons. It is shown using solar wind data from the WIND satellite, energetic electron data from the geostationary GOES satellites, and ground magnetometer data from the CANOPUS array, that the appearance of near-relativistic electrons near geostationary orbit follows increases in the solar wind pressure power in the ULF range. It is concluded that the ULF variations in solar wind pressure may magnetically pump the magnetosphere to increase the fluxes of energetic electrons to their observed levels near geostationary orbit.

Acknowledgements

I thank, most of all, my heavenly God and Father, for His majesty, glory and sovereignty over all things. He is the One who has created everything nearly as we see it around us and has given us the mandate to study our universe in Genesis 1:28 saying “*Be fruitful and multiply; fill the earth and subdue it; have dominion over the fish of the sea, over the birds of the air, and over every living thing that moves on the earth.*” He has also allowed me to complete this work to His glory and honour.

I thank my dear wife, Sylvia, for all her help, support, encouragement and love in the past few years and especially in the last weeks of completing this work.

I also thank Dr. G. Rostoker for his help in getting me into the program and for his persistence and his encouragements throughout this research. He has guided me in setting up my presentations and in the writing of this thesis. His helpful suggestions and guidance as my main supervisor throughout this research are most valuable to me. He has also financially supported me during most of this research. I also thank Dr. F. Fenrich for her helpful suggestions writing and completing the thesis work and in making the data more understandable and accessible. She has also financially supported me during the latter part of this research.

I also thank James Wanliss for his work in encouraging me and showing interest in this work. He was instrumental in increasing my interest in the space physics field and in getting me into the program. He provided much moral, physical and spiritual support during our time together in the lab.

The Space Environment Center (SEC) of NOAA provided the GOES energetic electron data. The CANOPUS instrument array provided the magnetometer data and was constructed and is operated by the Canadian Space Agency. K. Ogilvie and R. Lepping at NASA/GSFC have provided the WIND data used in this thesis via CDA Web.

Table of Contents

Dedication

Abstract

Acknowledgements

Table of Contents

List of Tables

List of Figures

List of Acronyms, Symbols and Units

1. Introduction	1
1.1 Space Environment	1
1.1.1 Solar Wind	1
1.1.2 Magnetosphere	2
1.2 Charged Particle Motion in a Magnetic Field	4
1.2.1 Adiabatic Invariants of Motion	6
1.3 Radiation Belts	8
1.4 Relativistic Electrons	11
1.5 Motivation	16
2. Theoretical Considerations	17
2.1 Adiabatic Acceleration	17
2.2 Radial Diffusion	18
2.3 The Recirculation Model	21

2.4	ULF Pulsations in Ground Based Magnetometer Data	23
2.5	The Toroidal-Mode Oscillation Model	29
2.6	The Compressional Wave Model	31
2.7	Thesis Direction	33
3.	Instrumentation and Data Analysis	35
3.1	Electrons near Geostationary Orbit	35
3.1.1	GOES	35
3.1.2	The GOES Energetic Particle Sensor	36
3.1.3	GOES Electron Data	39
3.2	Variations of the Solar Wind	40
3.2.1	WIND Satellite	40
3.2.2	Presentation of WIND Data	42
3.2.2.1	May 1998	45
3.2.2.2	January 1995	45
3.3	Event Definitions	46
3.4	Solar Wind Statistics	46
4.	Discussion and Conclusions	52
4.1	Counter Examples	52
4.1.1	Low Speed Wind Flows and Electron Enhancement	52
4.1.2	High ULF Power with No Electron Enhancement	54
4.1.3	No Pressure Power with Electron Enhancement	56
4.2	Other Considerations	56
4.2.1	Inward drifting Electron Gradients	56
4.2.2	High Energy Tail in the Electron Energy Spectrum	59
4.2.3	Instrument Thresholding	61
4.3	Concluding Remarks	61
Bibliography		64

List of Tables

Table	Page
3.1 GOES Satellite positions and time of local noon	35

List of Figures

Figure	Page
1.1 The complex structure of the Earth's magnetosphere. (Figure adapted from <i>Williams</i> , 1992.)	3
1.2 Three independent motions of a charged particle under the influence of a magnetic field. (a.) Gyration motion as a particle travels along a magnetic field line; (b.) Bounce motion as a particle travels between regions of higher magnetic field intensity; (c.) Drift motion as a particle travels perpendicular to the magnetic field. (Figure adapted from <i>Kivelson</i> , 1995.)	5
1.3 The loss cone. Charged particles with small pitch angle (α) may precipitate into the atmosphere whereas particles with a large pitch angle remain trapped by the magnetic field.	7
1.4 The left panel shows the equatorial omnidirectional electron flux at various electron energies and the slot region at approximately $L = 2.2 R_E$. The right panel shows the equatorial omnidirectional proton flux for various proton energies. Note that there is no slot region for the proton distribution. (Figure adapted from <i>Spjeldvik</i> , 1983.)	9
1.5 The Earth's magnetosphere showing the inner and outer radiation belts.	10
1.6 Characteristic appearance of Dst index data showing the main and recovery phases. This data is for the geomagnetic storm of March 11, 1998.	13

1.7	(a.) Electron drift path variation from the day side to the night side of the magnetosphere with the darker shading indicating higher energetic electron density. (b.) Diurnal variation in electron flux as measured near geostationary orbit. The measurement location is shown in the top panel. The electron flux data is measured by the GOES 7 satellite. In both panels, the position marked 'e' is local noon.	14
1.8	Energetic electron fluxes ($E > 2$ MeV) measured near geostationary orbit during the period of April 30 - May 15, 1998. The top bounding line shows the daily maximum at local noon and the lower curve shows the 5 minutes averaged data as measured by GOES 8.	15
2.1	Electron flux spectrum measured by the ISEE 1 satellite in the central plasma sheet at 13.4 RE during an active period on June 18, 1978 at 07:32 UT. (Figure adapted from <i>Christon et al.</i> , 1991.)	19
2.2	(a.) A time graph showing the changes in the total dayside magnetic field to cause radial diffusion. (b.) An initial state of the magnetosphere showing the initial drift path of the particles; (c.) when the magnetospheric magnetic field changes very quickly, causing the particles to violate the third adiabatic invariant, the dotted line shows the new drift path of the particles; (d.) as the magnetospheric magnetic field slowly relaxes to its original state, all three adiabatic invariants are conserved and some particles end up closer to the earth and some particles end up further from the earth. (Figure adapted from <i>Walt</i> , 1994.)	20

2.3	The recirculation model. (a.) Radial diffusion: conserving the first and second adiabatic invariants with energy gain; (b.) Pitch angle scattering: conserving energy while remaining on the same magnetic field line; (c.) Cross-L diffusion: conserving energy and the first adiabatic invariant; (d.) Pitch angle scattering: conserving energy while remaining on the same magnetic field line. (Figure adapted from <i>Fujimoto et al.</i> , 1990a.)	22
2.4	The CANOPUS magnetometer array	25
2.5	Raw magnetometer data measured at Gillam, MB on May 2, 1998 from 12:00 - 22:00 UT. Data measured with a sample rate of 0.2 Hz.	26
2.6	ULF pulsations in the magnetometer data measured at Gillam, MB on May 2, 1998 from 12:00 - 22:00 UT. Data is bandpassed from 1 - 10 mHz.	26
2.7	Energetic electron fluxes ($E > 2$ MeV) (drawn in the solid line) measured near geostationary orbit by GOES 7 and power in the ground based magnetometer data in the ULF frequency band (drawn in the dotted line) during a period of 92 days in 1994 at Gillam, MB. Gillam and GOES 7 are approximately in the same time zone.	27
2.8	Power in ULF pulsations (in the 0.8 - 20 mHz range) showing the longitudinal and latitudinal extent of the pulsations from April 21 (day 111) to May 31 (day 151) of 1998.	28

2.9	The toroidal-mode oscillation model. The solid arrows indicate the direction and magnitude of the radial electric field when the electron is at the location of the foot of the arrow. The open arrow indicates the direction of electron drift. Starting at dusk, the electron experiences a positive (radially outward) electric field and is transported radially earthwards and half a drift period later, the electron arrives at dawn, the electric field has become negative (radially inward) and causes the electron to be transported outwards. (Figure adapted from <i>Elkington et al.</i> , 1999.)	30
2.10	The compressional wave model. (a.) Radial diffusion: conserving the first and second adiabatic invariants with energy gain; (b.) Pitch angle scattering: conserving energy while remaining on the same magnetic field line; (c.) Radial diffusion: conserving the first and second adiabatic invariants with an energy loss. (Figure adapted from <i>Fujimoto et al.</i> , 1990a.)	32
3.1	The GOES satellite showing the south panel (to which the solar array is attached) bearing the HEPAD panel which contains the energetic particle sensors and the high energy proton and alpha detectors as part of the space environment monitor system instruments. (Figure adapted from <i>NASA</i> , 1996.)	37
3.2	The dome subassembly of the energetic particle sensor (EPS) on the GOES satellites. The three energy ranges (>0.55 , >2.0 and >4.0 MeV) are detected by three separate pairs of silicon surface barrier detectors and moderated by aluminum and copper of varying thicknesses. The dome subassembly is mounted on the HEPAD/EPS panel.	38

3.3	(a.) The WIND satellite, with all booms and instruments as deployed in space, showing the location of the solar wind experiment. The axis of rotation is vertical (+Z) in this diagram. At the indicated location, the Faraday Cup aims 15° below the equatorial plane and on the radially opposite side a second Faraday Cup aims 15° above the equatorial plane. (b.) WIND schematic showing the locations of the two Faraday Cups looking from the +Z shown in (i) and the looking from the -Y directions shown in (ii) (Figures adapted from <i>Ogilvie et al.</i> , 1995.)	41
3.4	Space conditions during the period of April 25 to May 10 of 1998. (a.) Solar wind proton number density, (b.) Solar wind speed; (c.) Hourly solar wind pressure power in the Pc 5 band; (d.) Energetic electron flux near geostationary orbit ($E > 2$) measured by GOES 8.	43
3.5	Space conditions for January 14 to February 11 of 1995. (a.) Solar wind proton number density, (b.) Solar wind speed; (c.) Hourly solar wind pressure power in the Pc 5 band. (d.) Energetic electron flux near geostationary orbit ($E > 2$) measured by GOES 7.	44
3.6	Space conditions for May 1998 (a.) Dst index; (b.) energetic ($E > 2$ MeV) electron flux (measured by GOES 8); (c.) Solar wind dynamic pressure power actual data (thin black line) and smoothed data (thick black line) for visual analysis.	47
3.7	The number of electron energization events with the given number of solar wind events with more dynamic pressure power than 10^{14} nPa ² /mHz during the period of January 1995 - December 1998.	48

3.8	(a.) Percentage of solar wind time periods which are associated with electron energization events as a function of peak power in the Pc5 frequency band of solar wind pressure variations. The power is computed on hourly intervals of solar wind dynamic pressure over the four year period from January 1995 to December 1998. The electron energization events are identified as sharp increases in the >2 MeV electron flux as measured near geostationary altitudes by GOES 8. (b.) The number of events used in the calculations of the top panel.	49
3.9	(a.) Distribution of solar wind speeds during an electron energization event during which the pressure power in the ULF band exceeded 10^{15} nPa 2 /mHz. (b.) Distribution of all solar wind speed data during the study time period of January 1995 - December 1998.	51
4.1	Space environment for May 13 to 23 of 1995. (a.) The low solar wind speed; (b.) the electron fluxes rising by nearly two orders of magnitude beginning on May 16; (c.) the dynamic solar wind pressure power which exceeded 10^{15} nPa 2 /mHz on May 16 and (d.) the Dst index for this time period for reference.	53
4.2	Space conditions from June 1 to 27, 1996. (a.) Solar wind speed; (b.) energetic ($E > 2$ MeV) electron flux measured by GOES 8; (c.) solar wind dynamic pressure power; (d.) Dst index and (e.) power in the ULF band calculated from ground based CANOPUS magnetometer data measured at Gillam, MB. The ULF power rises by more than one order of magnitude and yet the electron fluxes do not rise at all.	55

4.3	Space conditions for February 1996. (a.) Solar wind speed; (b.) electron flux measured by GOES 8; (c.) solar wind dynamic pressure power; (d.) Dst index and (e.) the power in the ULF band of 2-20 mHz from 12:00-20:00 UT measured at Gillam, MB.	57
4.4	Electron fluxes measured by GOES 8 for (a.) February 1996 and (b.) April and May 1998. On both plots, the dashed curve is the electron fluxes with ($E > 0.55$ MeV which is the lowest energy threshold of GOES 8) and the solid curve is the fluxes of electrons ($E > 2.0$ MeV). The solid line on each curve connects the daily maximum values near local noon for GOES 8. The higher energy electron flux plots show the same shape as the lower energy flux plots.	58
4.5	A schematic showing the high energy tail (no measured data) proposed by Onsager (solid curve) compared to the electron spectrum measured by the ISEE 1 satellite (dotted curve) also shown in Figure 2.1	60

List of Acronyms, Symbols and Units

α	pitch angle
\vec{B} , B	magnetic field
B_o	magnetic field at the equatorial plane
B_m	magnetic field at a mirror point in the ionosphere
CANOPUS	Canadian Auroral Network for the OPEN Program Unified Study
cm^2 , cm^3	units of area and volume, centimetres squared and cubed respectively
CPS	central plasma sheet
DC	direct current
DPU	data processing unit
$\delta\vec{r}$	small radial distance change
Dst	a geomagnetic storm index
e^-	electron
ε, λ	limiting quantity
\vec{E}	electric field
E	energy
ε_\perp	perpendicular kinetic energy
ε_\parallel	parallel kinetic energy
EPS	energetic particle sensor (on the GOES satellite)
\vec{F}	force
Φ_B	third adiabatic invariant
FFT	fast Fourier transform
GOES	Geostationary Operational Environmental Satellite
HEPAD	high energy proton and alpha detector (on the GOES satellite)
Hz	unit of frequency - Hertz
IMF	interplanetary magnetic field
ISEE	International Sun-Earth Explorer (a satellite)
ISTP	International Solar Terrestrial Physics
J	second adiabatic invariant

keV	unit of energy of a particle - kiloelectron volt
KHI	Kelvin-Helmholtz instability
km/s	speed unit - kilometres per second
ℓ	magnetic field line length
L	radial equatorial distance (commonly referred to as ‘L-shell’)
μ	first adiabatic invariant
MAG	magnetometer instrument (on the GOES satellite)
MeV	unit of energy of a high energy particle - megaelectron volt
MHD	magnetohydrodynamic
mHz	unit of frequency - milliHertz
mm, mm ²	length and area units- millimetre and millimetre squared, respectively
m_p	mass of the proton (1.673×10^{-27} kg)
mV/m	unit of electric field - millivolts per meter
n	particle number density
NASA	National Aeronautics and Space Administration
NGDC	National Geophysical Data Center
NOAA	National Oceanic and Atmospheric Administration
nPa	pressure unit - nanoPascal
nPa ² /mHz	pressure power unit - nanoPascal squared per milliHertz
nT	magnetic field unit - nanoTesla
OPEN	Origin of Plasma in Earth's Neighbourhood
P	solar wind dynamic pressure
p^+	proton
Pc 5	continuous pulsations in the frequency range of 2 - 7 mHz
q	charge
r	distance from Earth's centre (usually given in R_E)
R_E	Earth radius (= 6375 km)
s	unit of time - second
SAMPEX	Solar, Anomalous and Magnetospheric Particle Explorer (a satellite)
SAU	signal analyzer unit

SEC	Space Environment Center
SEM	space environment monitor
SOHO	Solar and heliospheric observatory (a satellite)
sr	unit of solid angle - steradian
SSBD	silicon surface barrier detector
SSC	sudden storm commencement
SWE	solar wind experiment (on the WIND space craft)
ULF	ultralow frequency
UT	universal time (based on the time at 0° geographic longitude)
\vec{v}	velocity
v_x	speed of the solar wind along the sun-earth line
v_{\perp}	particle velocity perpendicular to the magnetic field
v_{\parallel}	particle velocity parallel to the magnetic field
WIND	WIND spacecraft
XRS	X-Ray sensor (on the GOES satellite)
°	unit of angle - degrees

Chapter 1

Introduction

1.1 Space Environment

1.1.1 Solar Wind

Until the 1950's it was believed the interplanetary space was a vacuum. It was further thought that on occasion solar flares would lead to sudden ejection of gas from the sun. Magnetic storms were attributed to the effect of the incidence of these clouds of solar gas on the Earth's magnetic field [Chapman *et al.*, 1931]. Based on the observation of a dual cometary tail, *Biermann* [1951] proposed that, in addition to electromagnetic energy, the sun was continually emitting particles. A little later, *Parker* [1958] theoretically predicted the existence of this *solar wind* of particles, arguing that the flow of gas away from the sun was both supersonic and super Alfvénic. The presence of this solar wind was confirmed in the early 1960's by spacecraft observations. The reader is referred to *Isenberg*, [1991] for a full description of the solar wind and its origin.

The solar wind is, in fact, nothing more than the solar corona as it expands away from the sun enveloping the entire solar system. Typically the solar wind particles travel away from the sun with speeds of about 300 - 600 km/s, although from time to time the wind has been observed to drop to subsonic speeds and sometimes reaches speeds in excess of 1000 km/s. The wind is a nearly fully ionized plasma made up of mainly protons and electrons with average number densities of 1 - 10 particles/cm³ with occasional drops to about 0.1 particles/cm³ and rises to about 100 - 200 particles/cm³. The dynamic pressure of the solar wind is typically 1 - 10 nPa [Paschmann, 1991] which is well in excess of its thermal pressure.

The speed and density of the solar wind emanating from a region of the solar surface depends upon the solar magnetic field structure at that region. Regions of open magnetic field lines known as coronal holes produce faster, lower density solar wind streams while

regions of closed magnetic field lines known as coronal helmet streamers produce slower, higher density solar wind streams. The spatial variation of the solar magnetic field over the surface of the sun together with the solar rotation results in the large scale solar wind density and flow variations observed in the interplanetary medium. Superimposed on this background stream structure are sharper variations produced by transient events on the sun such as coronal mass ejections (CME's), erupting prominences, and solar flares. The high variability of the solar wind affects the space weather environment at the earth.

1.1.2 Magnetosphere

All planets which have a magnetic field (i.e. Mercury, Earth, Jupiter, Saturn, Uranus and Neptune) have that magnetic field distorted by the forces associated with the flow of the magnetized solar wind. The planetary magnetic fields and the charged particle populations trapped in those magnetic fields are referred to as planetary *magnetospheres*. The strength and orientation of the magnetic field of the planet affects the size and configuration of its magnetosphere. The Earth's magnetosphere was designed to protect life on Earth from the energetic particles moving through the interplanetary medium. In the absence of the solar wind, the magnetic field of the Earth is nearly dipolar with the field line geometry being much as one would observe around a bar magnet. The solar wind distorts this nearly dipolar magnetic field, with the frontside magnetic field lines being dragged back into the lee of the Earth to form the *magnetotail*. The shape of the magnetosphere as seen in Figure 1.1 is a consequence of the balance of the solar wind dynamic pressure from the outside and the magnetic field pressure inside; together with the effects of the interconnection of solar and terrestrial magnetic field lines through the process of field line merging and reconnection [Axford *et al.*, 1965].

The interaction between the solar wind and the magnetosphere leads to the production of magnetic storms and auroras, the latter being a conjugate phenomenon which can be observed simultaneously in both the northern and southern hemispheres. The magnetosphere cannot be observed visually but its physical character can be established

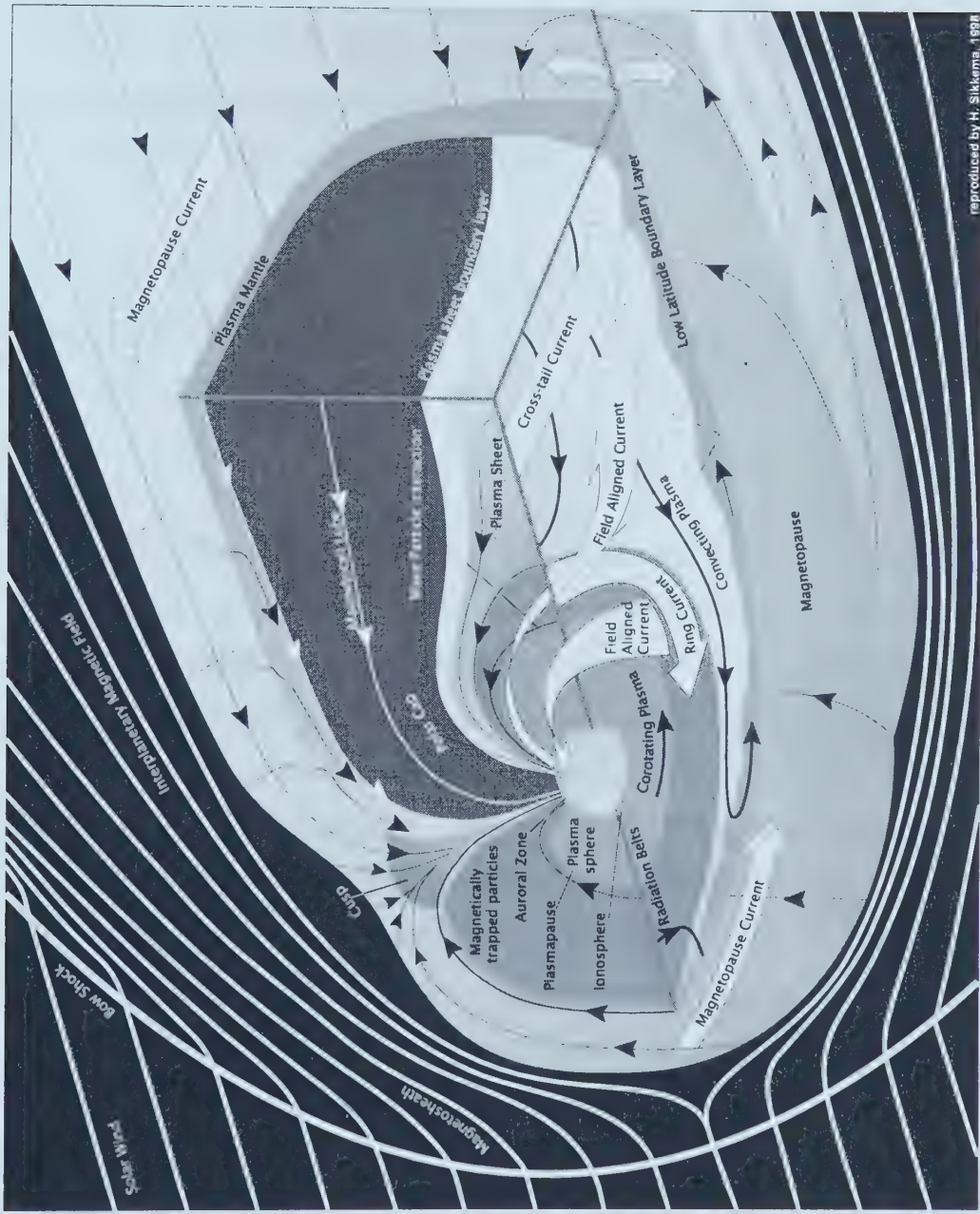


Figure 1.1 The complex structure of the Earth's magnetosphere. (Figure adapted from Williams, 1992.)

from magnetometers and particle detectors flown on satellites and by various types of remote sensing instrumentation located on the ground. The sunward boundary of the Earth's magnetosphere is located at about $10 R_E$ ($1 R_E = 6375$ km which is the Earth's radius) from the centre of the planet at the noon meridian, while the magnetotail stretches to well beyond $200 R_E$ on the nightside [Speiser, 1991]. In fact, the magnetic signature of the magnetotail has been detected up to a distance of about $1000 R_E$ from the Earth by the Pioneer 7 spacecraft [Fairfield, 1968].

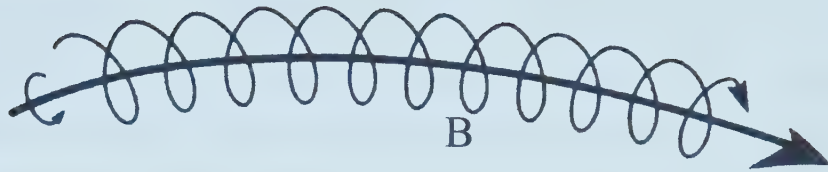
1.2 Charged Particle Motion in a Magnetic Field

Charged particle motion, in the presence of an electromagnetic field, is understood to follow the Newton-Lorentz force law:

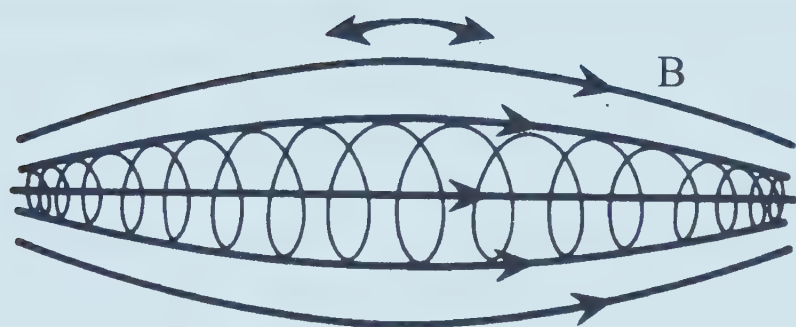
$$\vec{F} = q(\vec{v} \times \vec{B} + \vec{E})$$

In the magnetosphere, this behaviour is manifested in three different types of motion on three different time scales. On the shortest time scale, charged particles move in a circular or helical motion around magnetic field lines with the actual time scale depending on the particle's charge, mass and energy. For electrons and protons of a few keV at geostationary orbit, the periods of gyration are on the order of a few tenths of a millisecond and a few tenths of a second respectively. The second timescale involves the motion of a charged particle along magnetic field lines and in particular the bouncing of the particles between regions of higher magnetic field intensity in the north and south hemispheres. The bounce time, on magnetic field lines crossing the equatorial plane at geostationary orbit, for electrons and protons of a few keV is of the order of a few tenths of a second and a few tens of seconds respectively. The third time scale involves azimuthal drift in a direction perpendicular to the magnetic field lines, tracing out a closed shell around the Earth. The drift time, on a shell crossing the equatorial plane at geostationary orbit, for electrons and protons of a few keV is on a timescale of hours. The motions of charged particles in the Earth's magnetic field, as described above, is shown in Figure 1.2 [Kivelson, 1995].

(a.)



(b.)



(c.)

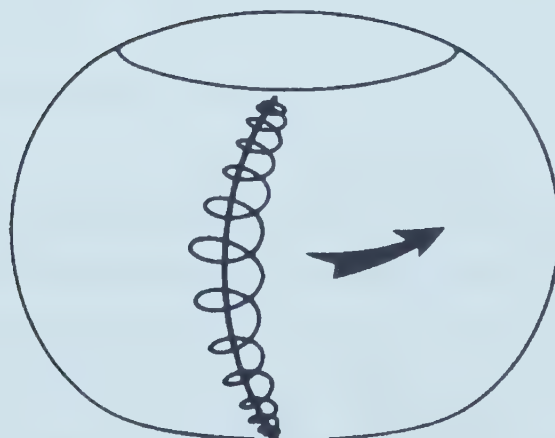


Figure 1.2 Three independent motions of a charged particle under the influence of a magnetic field. (a.) Gyration motion as a particle travels along a magnetic field line; (b.) Bounce motion as a particle travels between regions of higher magnetic field intensity; (c.) Drift motion as a particle travels perpendicular to the magnetic field. (Figure adapted from *Kivelson*, 1995.)

The motion of a charged particle is helical in character so that the particle velocity can have components parallel and perpendicular to the magnetic field (v and v_{\perp} respectively). The pitch of the helix is described by the pitch angle of the particle (α), where α is defined by $\tan(\alpha) = \frac{v_{\perp}}{v_{\parallel}}$. When a particle has a small pitch angle ($v_{\parallel} \gg v_{\perp}$) in the equatorial plane, it may approach Earth reaching altitudes of less than 1000 km. At these altitudes the particle may collide with atmospheric particles becoming no longer trapped and is said to have *precipitated* into the atmosphere. The limiting pitch angle depends on the magnitude of the magnetic field at the point of the bounce since for a bounce to occur, the pitch angle approaches 90° as v_{\perp} approaches zero and upon reflection, v_{\perp} increases in the opposite direction. The loss cone angle, as shown in Figure 1.3, in the equatorial plane is defined by $\sin^2(\alpha_o) = \frac{B_o}{B_m}$ where B_m is the magnetic field at the mirror point in the ionosphere and B_o is the magnetic field at the location where the loss cone angle is calculated. At an equatorial distance of $6 R_E$, a charged particle which will precipitate at an altitude of about 100 km is inside the loss cone of about 4° , which means that any charged particle with a pitch angle of less than 4° , at an equatorial distance of about $6 R_E$, will precipitate into the atmosphere around or below 100 km in altitude and probably not mirror back into the magnetosphere [Schulz, 1991].

1.2.1 Adiabatic Invariants of Motion

The three previously mentioned motions (*i.e.* gyrotrational, bounce and drift) combine to give a charged particle in the Earth's magnetic field a very complex trajectory. The study of charged particle motions is made easier by the appropriate choice of reference frame, and in the case of space plasma, the guiding centre frame is found to be very useful. The origin of this reference frame is the centre of gyration of the particles as it orbits the magnetic field line. Working in this reference frame, one can define three invariants of the motion subject to specific constraints in terms of time variations in the background magnetic field. These are called *adiabatic invariants*, and are described as follows.

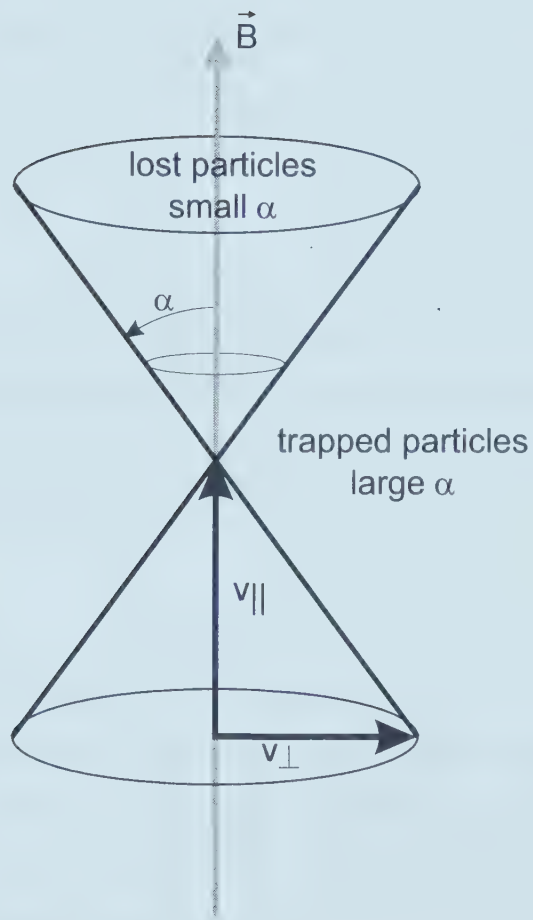


Figure 1.3 The loss cone. Charged particles with small pitch angle (α) may precipitate into the atmosphere whereas particles with a large pitch angle remain trapped by the magnetic field.

The first adiabatic invariant deals with the gyration of the particle around the guiding centre. When the magnetic field changes slowly compared to the time to complete one gyration, then the magnetic moment, $\mu = \frac{\mathbf{e}_\perp}{B}$ (perpendicular kinetic energy divided by the magnetic field strength) is conserved.

The second invariant deals with the bounce motion of a trapped particle. When the magnetic field changes slowly compared to the time to complete one bounce cycle, then the product of parallel kinetic energy and the square of the field line length ($J = \langle e \rangle \ell^2$) is conserved.

The third invariant deals with the drift motion perpendicular to the Earth's magnetic field lines. When the magnetic field changes slowly compared to the time for a particle to drift around the Earth then the total magnetic flux (Φ_B) enclosed by the drifting particle as it drifts around the Earth will be conserved.

1.3 Radiation Belts

The magnetosphere is filled with a plasma of mainly protons and electrons. In 1958, James Van Allen used data from the Explorer IV spacecraft to show that there are two regions of high-energy electrons in the magnetosphere which became known as the *inner* radiation belt and the *outer* radiation belt. Although there is a continuous belt of lower energy radiation filling the entire magnetosphere, high energy ($E > 10$ MeV) protons and high energy ($E > 0.5$ MeV) electrons are concentrated in the inner belt and electrons of energies of up to a few MeV are concentrated in the outer belt. The distribution of electrons out to about $3 R_E$ and protons out to about $5 R_E$ are shown in Figure 1.4 and the location of radiation belts are shown in Figure 1.5.

The inner radiation belt forms when very high energy cosmic rays enter the magnetosphere and collide with atoms in the atmosphere. When a cosmic ray particle collides with the nucleus of an atmospheric atom, high energy neutrons are created and

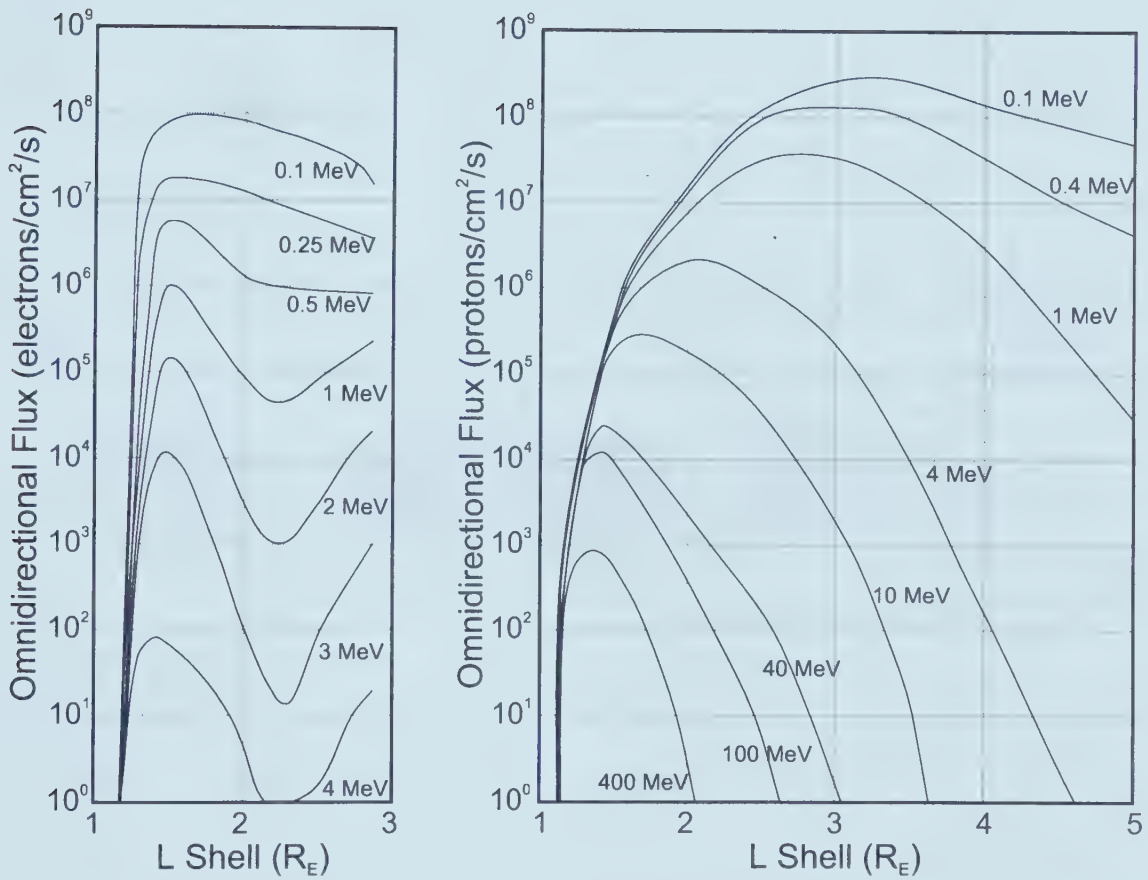


Figure 1.4 The left panel shows the equatorial omnidirectional electron flux at various electron energies and the slot region at approximately $L = 2.2 R_E$. The right panel shows the equatorial omnidirectional proton flux for various proton energies. Note that there is no slot region for the proton distribution. (Figure adapted from *Spjeldvik*, 1983.)

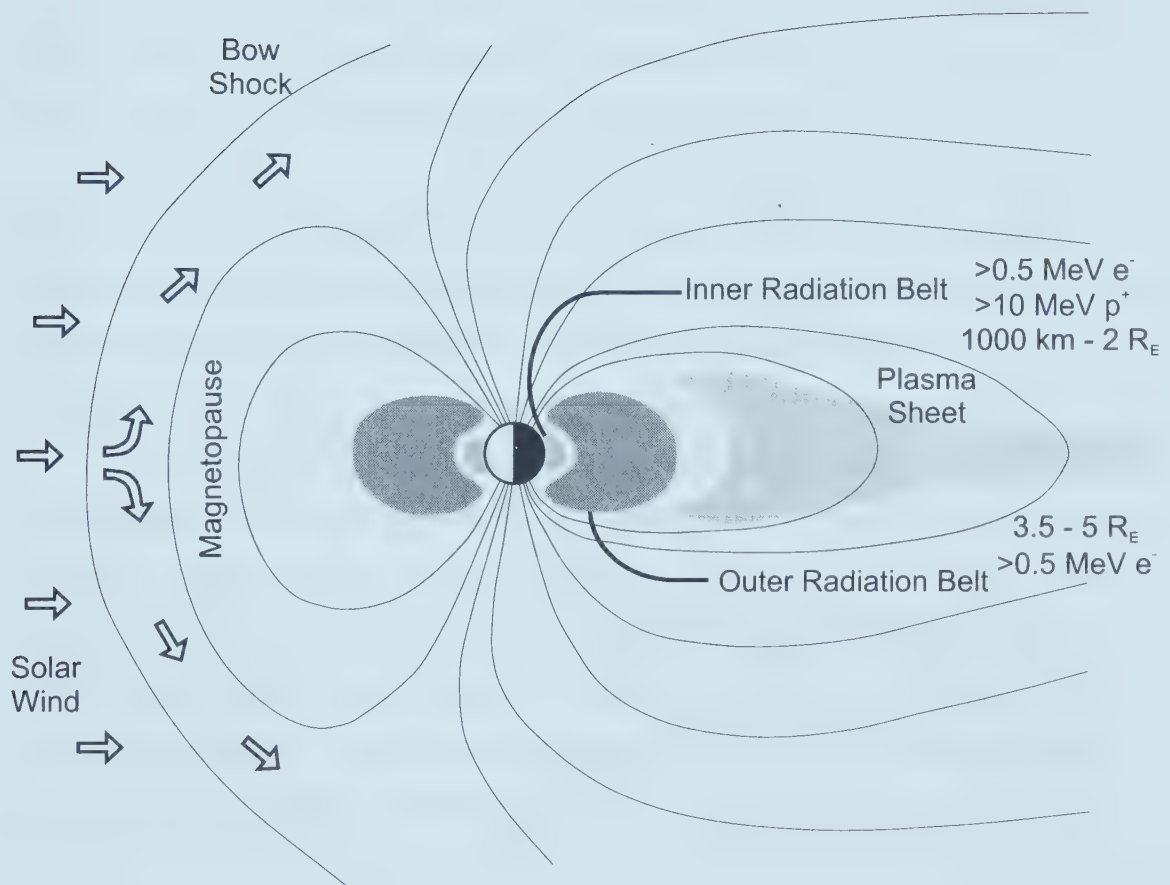


Figure 1.5 The Earth's magnetosphere showing the inner and outer radiation belts.

some directly escape the atmosphere. Some of these neutrons spontaneously decay into a proton, an electron and a neutrino in a region of the magnetosphere where the magnetic field can trap some of the new charged particles, with sufficiently low velocities, to form the inner radiation belt. The equatorial crossing point range of the inner belt is about from 1000 km in altitude to about $2.2 R_E$ from the Earth's centre. The protons in this region have energies up to a few hundred MeV and the electrons have energies up to a few MeV. The outer boundary of the inner radiation belt is indicated by a local minimum (near $L = 2.2$) in the 1 MeV electron flux radiation intensity. [Van Allen *et. al.*, 1958; Van Allen and Frank, 1959; Schulz, 1991; Spjeldvik; 1983].

The outer radiation belt is produced by injection and energization events associated with magnetic storms and involves earthward radial diffusion of plasma sheet particles. In the plasma sheet at around $20 R_E$ behind the earth, the more energetic electrons have energies of about 1 keV and the protons have energies of about 10 keV [Parks, 1991; Coon, 1966]. The electrons are accelerated to much higher energies as they diffuse and move earthward to become part of the outer radiation belt. The outer radiation belt is dominated by electrons of energies of several hundred keV to a few MeV and protons of energies of a few MeV [Walt, 1994]. The equatorial crossing point range outer radiation belt is approximately $3\frac{1}{2} R_E$ to about $5 R_E$ from the earth's centre. During magnetic storms, the outer radiation belt can extend well beyond $6 R_E$ from the earth's centre into the region of geostationary orbit and beyond.

1.4 Relativistic Electrons

The charged particles in the radiation belts drift in opposite directions due to their opposite charges and produce a ring current around the earth. Alexander von Humboldt (1769-1859) detected changes in this ring current by measuring the earth's magnetic field and noted that these changes were essentially identical all over the world. He called these ring current increases *magnetic storms*. Typically, a storm takes about half a day to develop in what is called the *main phase*, and it gradually decays over the next few days

in what is called the *recovery phase*. Small magnetic storms, with disturbances between 50 and 300 nT, occur about 30 - 40 times yearly [Russell *et al.*, 1973]. When the storm occurs, there is an injection of energetic ions and electrons from the magnetotail, causing the ring current to strengthen significantly. The *disturbance storm time* (Dst) index is a measure of geomagnetic activity used to assess the severity of magnetic storms. It is based on the average value of the horizontal component of the Earth's magnetic field measured hourly at four near-equatorial geomagnetic observatories. Use of the Dst as an index of storm strength is possible because the strength of the surface magnetic field at low latitudes is inversely proportional to the energy content of the ring current, which increases during geomagnetic storms. In a magnetic storm the interplanetary magnetic field (IMF) turns southward and the Dst shows a sharp decrease as the ring current intensifies in the main phase of the storm as shown in Figure 1.6. Once the IMF turns northward again and the ring current begins to recover, the Dst begins a slow rise back to its quiet time level during the storm's recovery phase. Other currents contribute to the Dst as well, most importantly the magnetopause current. The Dst index may be corrected to remove the contribution of this current as well as that of the quiet-time ring current. Geomagnetic storms can affect radio communication, satellite operations and even the safety of astronauts in Earth orbit.

It is these effects, associated with magnetic storms, which have recently increased the interest in the energization of electrons to relativistic energies, a process which is not fully understood today. Since the electrons travel from the day side of the magnetosphere around to the night side and back to the day side, the electron flux has a diurnal fluctuation due to the stretched field lines on the night side. That is, energetic electrons are less dense on the night side due to the particle motion conserving the third adiabatic invariant and spreading out further away from the Earth as shown in Figure 1.7. Near geostationary orbit, the day side energetic electron fluxes ($E > 2$ MeV) can rise very rapidly. The time for the energetic electron fluxes to be enhanced to relativistic energies near geostationary orbit is typically about 8-10 hours as shown in Figure 1.8. Initially the

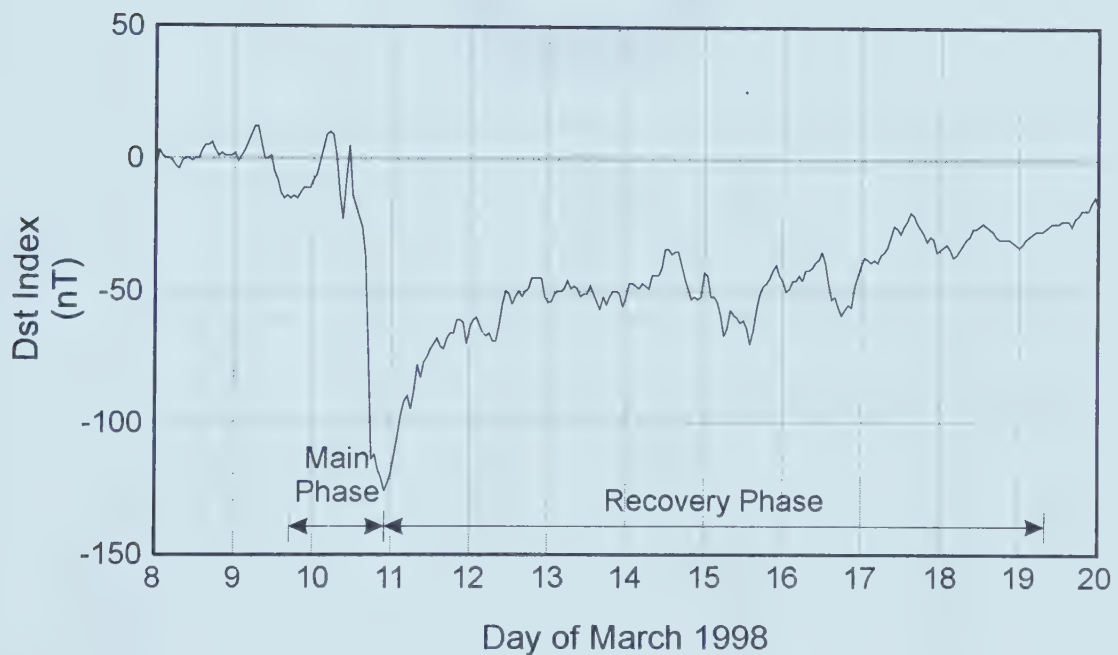
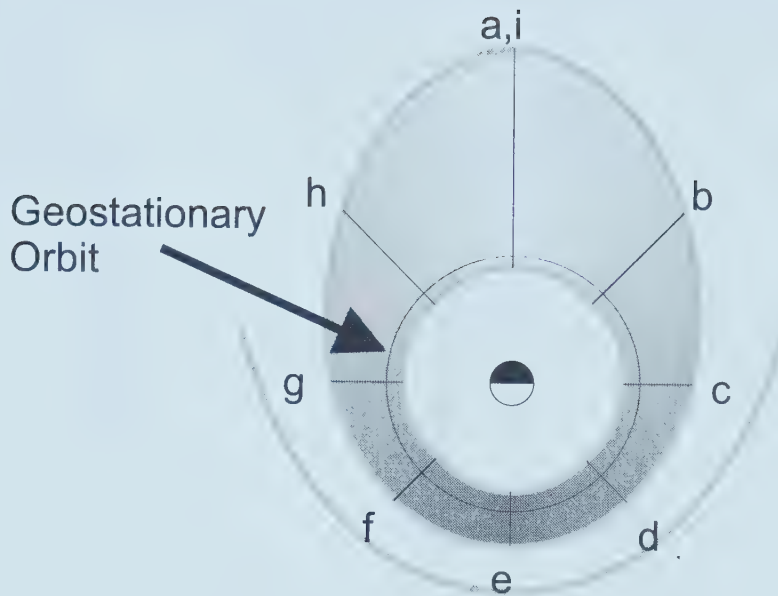


Figure 1.6 Characteristic appearance of Dst index data showing the main and recovery phases. This data is for the geomagnetic storm of March 11, 1998.

(a.)



Solar Wind

(b.)

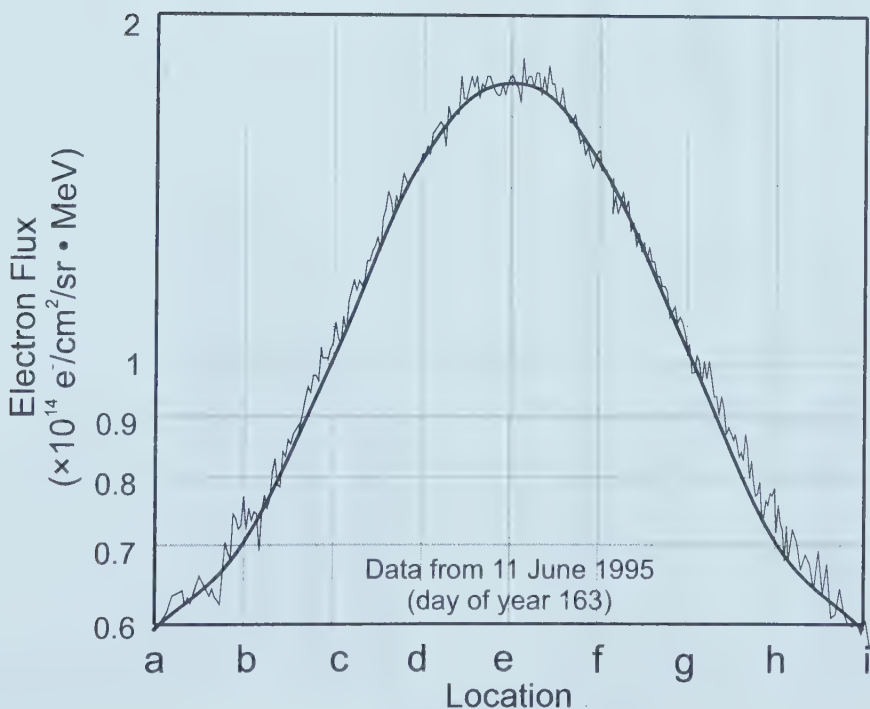


Figure 1.7 (a.) Electron drift path variation from the day side to the night side of the magnetosphere with the darker shading indicating higher energetic electron density. (b.) Diurnal variation in electron flux as measured near geostationary orbit. The measurement location is shown in the top panel. The electron flux data is measured by the GOES 7 satellite. In both panels, the position marked 'e' is local noon.

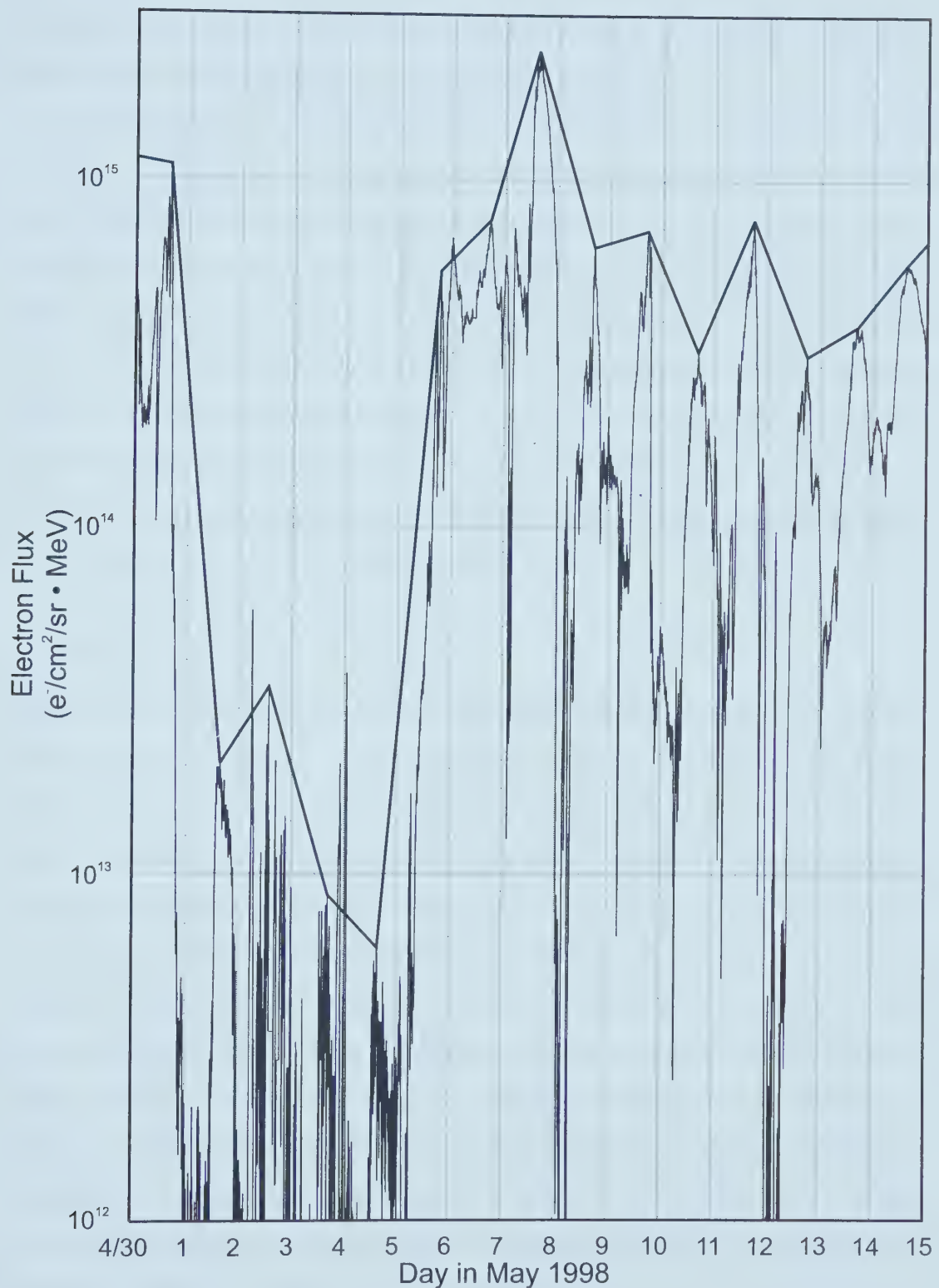


Figure 1.8 Energetic electron fluxes ($E > 2$ MeV) measured near geostationary orbit during the period of April 30 - May 15, 1998. The top bounding line shows the daily maximum at local noon and the lower curve shows the 5 minutes averaged data as measured by GOES 8.

electron fluxes drop out for a short period of time, at the time of a magnetic storm onset, before there is a very large increase in electron count. This is due, in part, to the fact that the magnetosphere is highly disturbed and the third adiabatic invariant is no longer conserved. The electrons are likely being energised but near geostationary altitudes the particle orbits around the earth are open and the electrons are lost to the plasma sheet on their orbit through the night side of the magnetosphere. Secondly, after the main phase of the magnetic storm concludes, the electron flux rises *very* quickly — over a time span of a few hours (8-10 hours). The electrons appear to be energised over a broad L-shell range between the magnetopause (about $L = 10$) and the average position of the outer edge of the outer radiation belt (about $L = 5$) as shown by *Rostoker et al.* [1998]. The appearance of strongly enhanced energetic electron fluxes is a problem of great interest and is being addressed by many researchers world wide.

1.5 Motivation

Satellite observations have shown that near relativistic electron fluxes near geostationary orbit can rise very quickly. The primary motivation for this thesis is that satellite operations can be impaired, affecting many aspects of life here on Earth, when these fluxes sharply rise. As an example, after more than two weeks of elevated energetic electron fluxes in January 1994, on January 20 at 17:35 UT the Anik E1 (which provided a broad range of video, voice, and data services across North America) suffered severe malfunctions which, through laboratory testing, were shown to be a result of the space environment [*Baker et al.*, 1996]. During the next few years, with the ever increasing number of satellites near geostationary orbit, it will be important to better understand the space environment and thus to determine how spacecraft can withstand the effects of enhanced energetic particle fluxes. A second motivation for this thesis work is to more fully understand the process of rapid electron energization near geostationary orbit as one of the many complex processes in the magnetosphere.

Chapter 2.

Theoretical Considerations

2.1 Adiabatic Acceleration

In adiabatic acceleration, there is an energy gain due to the stronger magnetic field and shorter field line length near the Earth. This energy gain is realized through the conservation of the first and second adiabatic invariants in a process known as betatron and Fermi acceleration respectively.

Betatron acceleration involves the conservation of the first adiabatic invariant ($\mu = \frac{\epsilon_{\perp}}{B}$); the perpendicular energy (ϵ_{\perp}) is inversely proportional to the cube of the equatorial radial distance (r) since $B \propto r^{-3}$ (assuming a near dipolar magnetic field). Using $\epsilon_{\perp,i}$ as the initial energy of the electron on an outer magnetic field line at a radial distance of r_i , after the earthward transport to an inner magnetic field line at a radial distance of r_f , the final energy of the electron ($\epsilon_{\perp,f}$) is approximated as

$$\epsilon_{\perp,f} = \left(\frac{r_i}{r_f}\right)^3 \cdot \epsilon_{\perp,i}$$

Fermi acceleration involves the conservation of the second adiabatic invariant ($J = \langle \epsilon_{\parallel} \rangle \ell^2$, where ℓ is the field line length). Assuming a near dipolar magnetic field, the field line length (ℓ) is proportional to the equatorial radial distance (r). Thus the average parallel energy of a small pitch angle electron ($\langle \epsilon_{\parallel} \rangle$), being inversely proportional to the square of the equatorial radial distances, is approximated as

$$\langle \epsilon_{\parallel,f} \rangle = \left(\frac{r_i}{r_f}\right)^2 \cdot \langle \epsilon_{\parallel,i} \rangle$$

Figure 2.1 shows the energy dependence of electron flux in the central plasma sheet (CPS) at $13.4 R_E$ during an active period as measured by ISEE 1. Although an average active CPS electron with an energy of about 2 keV is considered in the following, the possibility of energizing the smaller population of higher energy electrons is briefly discussed later in the final chapter of this thesis. Considering the above approximate relations, when a CPS electron at about $10 R_E$ is transported to a distance of $4 R_E$, the energy increases by a factor of about 15.6 due to betatron acceleration and by about 6.3 due to Fermi acceleration. The maximum resulting energy of a 2 keV electron from the CPS is approximately 35 keV.

Therefore the standard acceleration mechanisms of conserving adiabatic invariants are clearly not enough to produce the observed fluxes of relativistic electrons in the 1-2 MeV range when normal energy plasma sheet particles convect earthwards and begin to radially diffuse. Instead, either very high energy particles must come from the plasma sheet or another mechanism or mechanisms must come into play to produce the observed high energy fluxes. In the following four sections we investigate several possible explanations of the appearance of near relativistic electrons near geostationary orbit.

2.2 Radial Diffusion

Radial diffusion is a term for the process of changing the radial distribution of trapped charged particles [Walt, 1994]. It is necessary for the formation of the outer radiation belt and can redistribute particles which are injected and energized by magnetic storms by bringing some of those particles closer to the Earth. For this to occur, the electric or magnetic field must change on a timescale faster than the time for the charged particle to drift once around the Earth. The drift time, on a shell crossing the equatorial plane at geostationary orbit, for electrons and protons of a few keV is on a timescale of hours. In this discussion we will only consider the magnetic field variations. When the magnetic field changes on a timescale faster than the drift period but slower than the bounce period ($t_{\text{Drift}} > t_{\Delta B} > t_{\text{Bounce}}$) (Figure 2.2a,c), the third invariant (Φ_B) will be violated but the

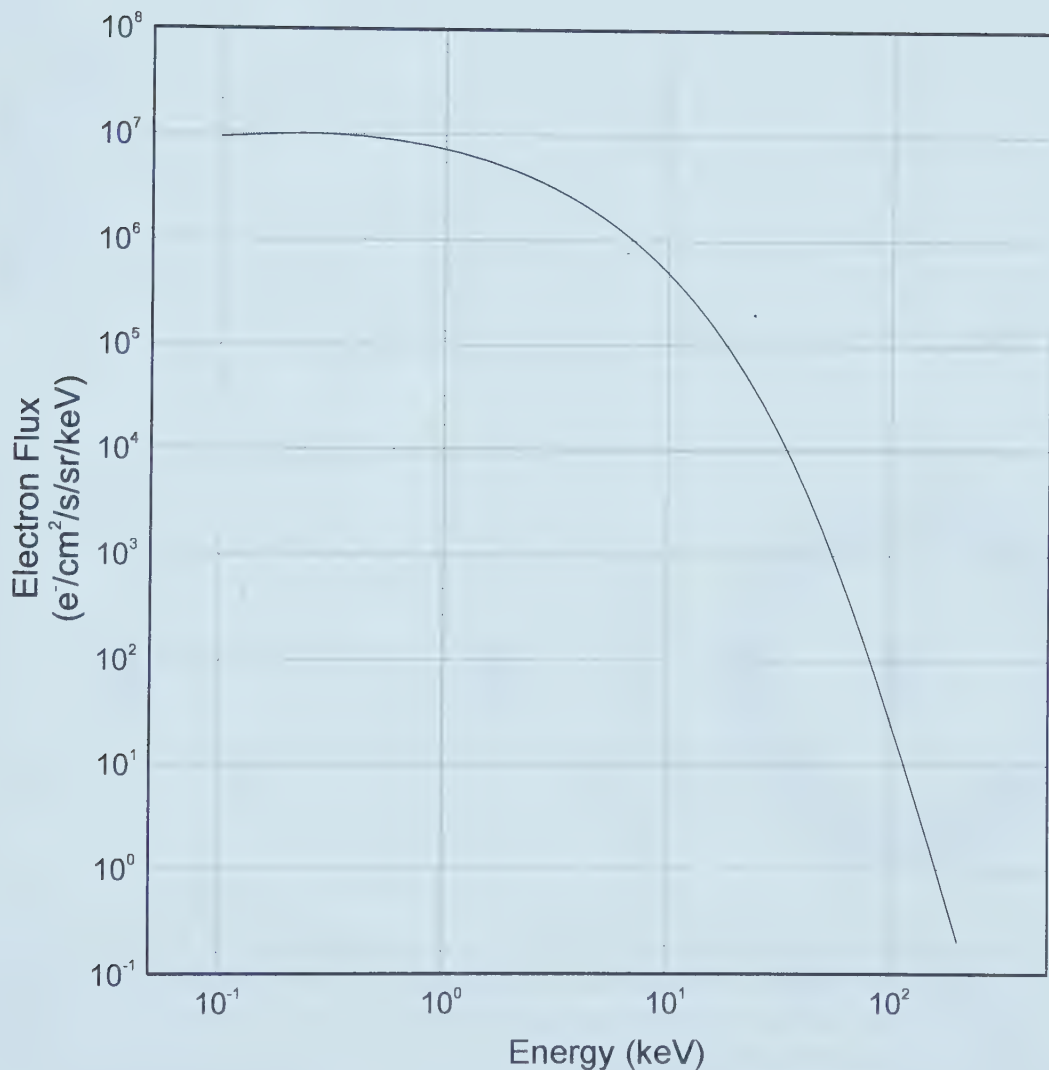


Figure 2.1 Electron flux spectrum measured by the ISEE 1 satellite in the central plasma sheet at $13.4 R_E$ during an active period on June 18, 1978 at 07:32 UT. (Figure adapted from *Christon et al.*, 1991.)

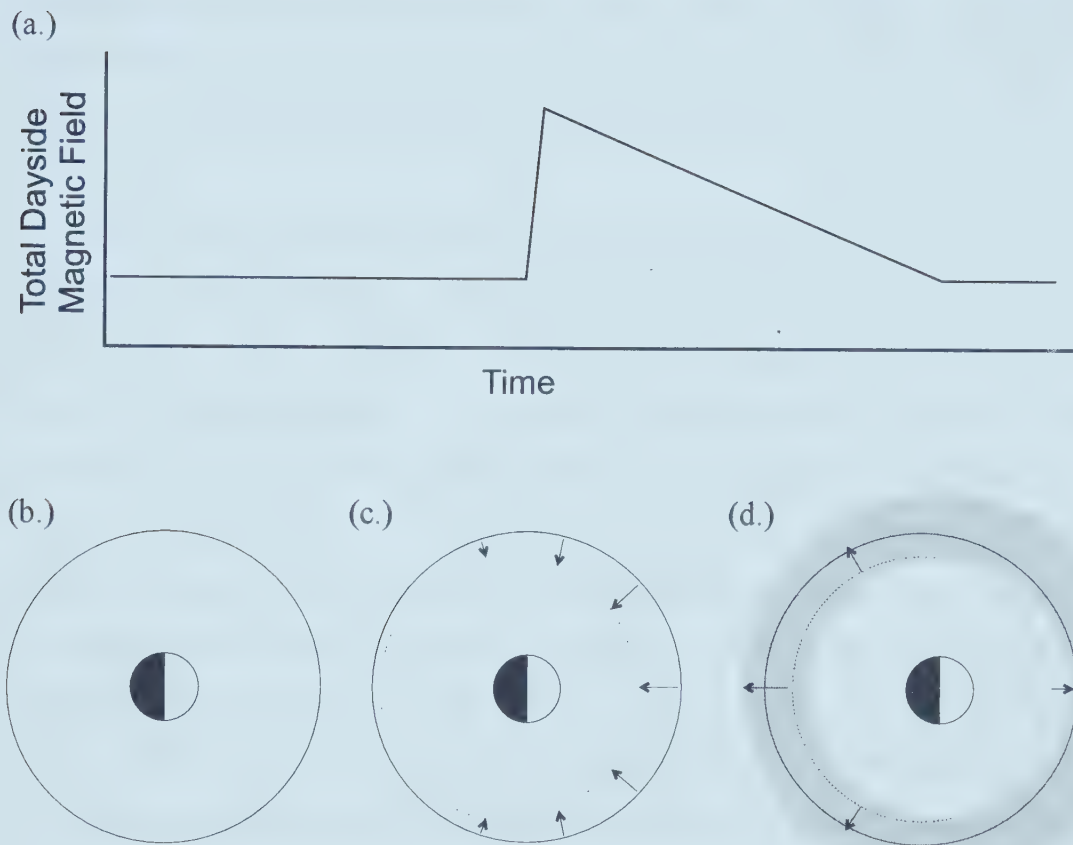


Figure 2.2 (a.) A time graph showing the changes in the total dayside magnetic field to cause radial diffusion. (b.) An initial state of the magnetosphere showing the initial drift path of the particles; (c.) when the magnetospheric magnetic field changes very quickly, causing the particles to violate the third adiabatic invariant, the dotted line shows the new drift path of the particles; (d.) as the magnetospheric magnetic field slowly relaxes to its original state, all three adiabatic invariants are conserved and some particles end up closer to the earth and some particles end up further from the earth. (Figure adapted from *Walt, 1994.*)

first (μ) and second (J) invariants will be conserved. Thus when the magnetosphere slowly relaxes to its original state (Figure 2.2d), the new values of the third invariant will be conserved. The particles will spread out in radial distance as the magnetosphere relaxes and all three of the invariants will be conserved — some particles will come closer to the Earth and some will diffuse outwards, further from Earth (Figure 2.2d) relative to their original trajectory. The particles which diffuse closer to Earth are accelerated and may become trapped to form the outer radiation belt [Walt, 1994].

The energization possible by the betatron and Fermi acceleration associated with radial diffusion is seen in the sudden storm commencement (SSC) of March 24, 1991. In this event, the formation of a new electron radiation belt was observed. *Li et al.* [1993] note that the interplanetary shock was a bipolar electric field pulse with peak to peak magnitude of 80 mV/m and monopolar magnetic pulse with peak to peak magnitude of 140 nT which lasted about 120 seconds. This shock and the formation of the new radiation belt was simulated by *Li et al.* [1993] and was estimated to have compressed the magnetosphere from $10 R_E$ probably to about $4 R_E$ in less than 100 seconds and to have energized electrons up to about 50 MeV. This new radiation belt was observed to persist for at least six months. Although this was a unique event, it does demonstrate that such dramatic energization is possible by rapid inward radial transport using only a single solar wind impulse.

2.3 The Recirculation Model

The Nishida recirculation model [Nishida, 1976] applies the radial diffusion method numerous times in sequence to achieve the total electron acceleration required to explain the observations. This model describes a method of bringing an electron from an outer magnetic field line inwards and subsequently back to the outer magnetic field line again without losing an appreciable amount of energy in the return. Figure 2.3 shows the four diffusive processes in this recirculation model: inwards radial diffusion, pitch angle diffusion, low-altitude cross-L diffusion and further pitch angle diffusion. Both pitch

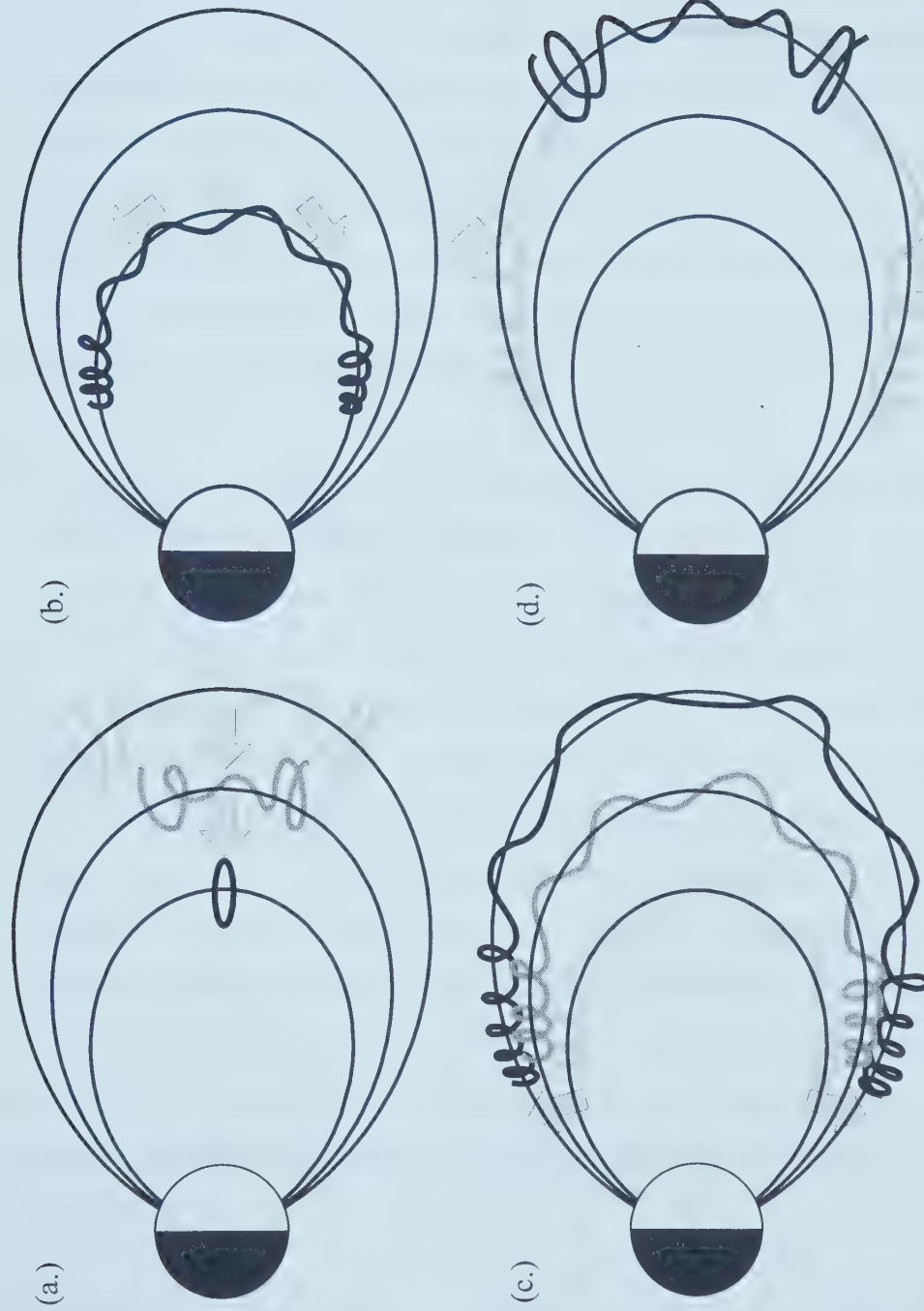


Figure 2.3 The recirculation model. (a.) Radial diffusion: conserving the first and second adiabatic invariants with energy gain; (b.) Pitch angle scattering: conserving energy while remaining on the same magnetic field line; (c.) Cross-L diffusion: conserving energy and the first adiabatic invariant; (d.) Pitch angle scattering: conserving energy while remaining on the same magnetic field line. (Figure adapted from *Fujimoto et al.*, 1990a.)

angle diffusive processes(Figures 2.3b and d) in this model involve a very small energy change. The cross-L diffusion (Figure 2.3c) also involves a very small energy change due to the small change in magnetic field at low altitudes [*Fujimoto et al.*, 1990a, b]. The radial diffusive process (Figure 2.3a) conserves the first and second adiabatic invariants whereas both instances of pitch angle scattering conserve energy while the particle remains on the same L-shell. Cross-L diffusion conserves both energy and the first adiabatic invariant since the change in magnetic field is small at low altitudes. The only energy change is realized by the inward radial diffusion. Thus by exposing the electrons to this circulation process numerous times, with a small energy gain over each cycle, the electron can attain the energies observed.

The main difficulty with the Nishida recirculation model is the timing of the appearance of the energetic electron fluxes. *Fujimoto et al.* [1990b] note that the electron population in the energy range above 1 MeV is significantly enhanced after a few days from the start of the energization process. *Baker et al.* [1989] show that an electron diffusing from $L = 8$ to 6.6 , increases the energy by a factor of 1.8 and the time to radially diffuse is about 0.4 days. Additionally, the low-altitude cross-L diffusion requires about one day [*West et al.*, 1981]. Thus to energise a 10 keV plasma sheet electron to 1 MeV would require about 8 cycles to be completed and thus a total time of more than 14 days is required — far longer than we observe in the magnetosphere [*Liu et al.*, 1999]. In observations from the GOES 7, 8 and 10 satellites (Figure 1.8) we see that the fluxes of electrons in the energy range above 2 MeV rise sharply over a period of about 8 - 10 hours. Thus we can clearly see that the Nishida recirculation model is not sufficient to explain the sudden appearance of enhanced fluxes of near relativistic electrons at geostationary orbit.

2.4 ULF Pulsations in Ground Based Magnetometer Data

In searching for the source of the energetic electrons near geostationary orbit, *Rostoker et al.* [1998] note that the appearance of energetic electrons follows the

appearance of large amplitude ultra low frequency (ULF) magnetic pulsations. These ULF pulsations were detected using the ground based magnetometer array of CANOPUS in north-central to north-western Canada (a map showing the magnetometer locations is shown in Figure 2.4) These ULF pulsations have frequencies of 2-7 mHz (periods of about 2-10 minutes) and are classified as Pc 5 pulsations [Jacobs *et al.*, 1964]. An example of these pulsations is shown in Figure 2.5 which displays a magnetogram measured at Gillam, Manitoba. Figure 2.6 displays the magnetometer data filtered to show only the pulsation activity in the ULF frequency band of 1 - 10 mHz.

The power in the ULF pulsations in the Pc 5 band maximizes between local dawn and local noon [Gupta, 1976]. Figure 2.7 clearly shows that in nearly every instance, the ULF pulsation power increases prior to the rise in relativistic electron fluxes [Rostoker *et al.*, 1998]. This leads to the idea that the ULF pulsations may be associated with the electron acceleration process. In looking at the distribution of the ULF pulsation energy, we can see from Figure 2.8 that when the ULF pulsation power at one of the CANOPUS stations rises, in general the power at the other stations rises. This shows the very broad longitudinal and latitudinal extent of the ULF pulsation source region, across the entire morning sector of the magnetosphere and ionosphere system.

One possibility for the production of ULF pulsations is in the Kelvin-Helmholtz instability (KHI) along the flanks of the magnetosphere. Along the morning sector flank, there is velocity shear between the magnetosheath plasma and the plasma sheet plasma permitting boundary surface waves to develop. These surface waves can couple to compressional waves which propagate earthward as fast mode disturbances. Some of the energy from the compressional waves can then couple into shear Alfvén waves which can be detected on the ground as Pc 5 magnetic pulsations. Even during periods of constant solar wind speed, the KHI can lead to the development of compressional waves: the pulsation power is observed to be higher during periods of high solar wind speed. [Wolfe *et al.*, 1980].



Figure 2.4 The CANOPUS magnetometer array

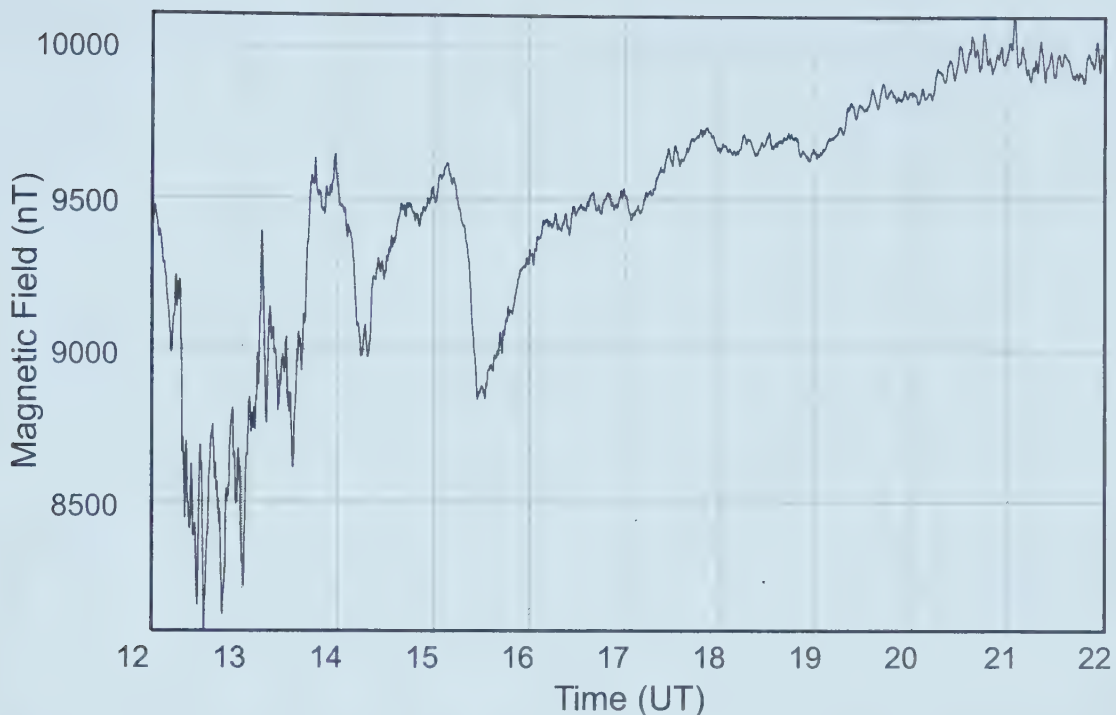


Figure 2.5 Raw magnetometer data measured at Gillam, MB on May 2, 1998 from 12:00 - 22:00 UT. Data measured with a sample rate of 0.2 Hz.

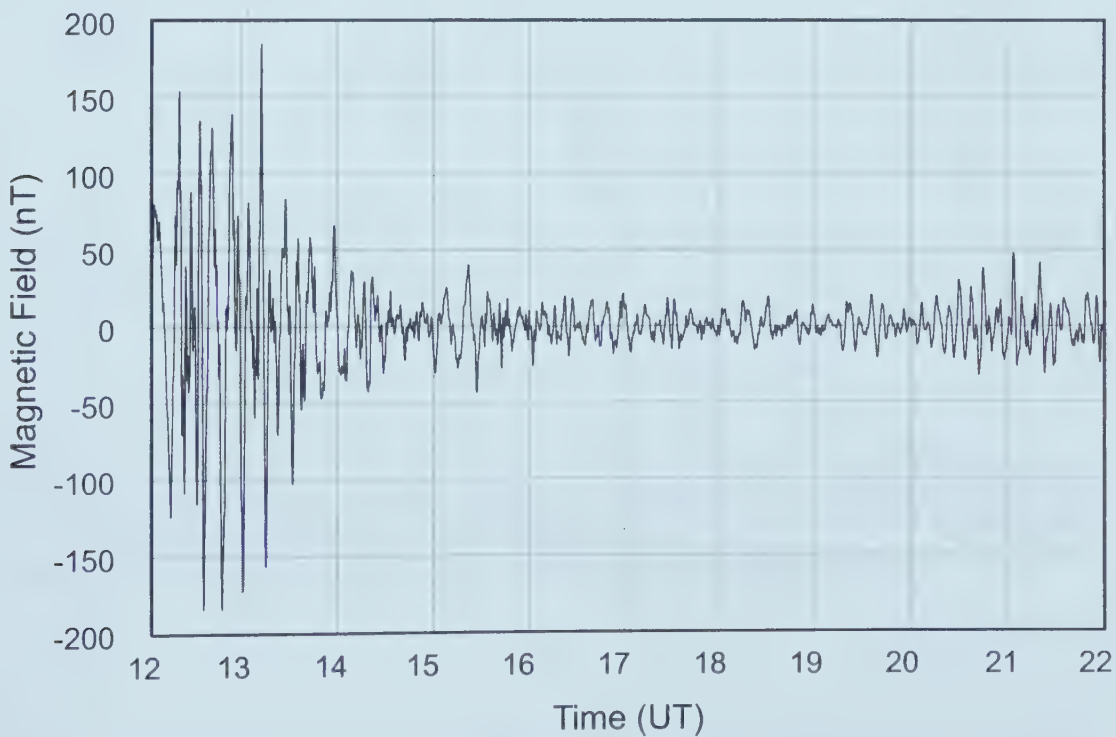


Figure 2.6 ULF pulsations in the magnetometer data measured at Gillam, MB on May 2, 1998 from 12:00 - 22:00 UT. Data is bandpassed from 1 - 10 mHz.

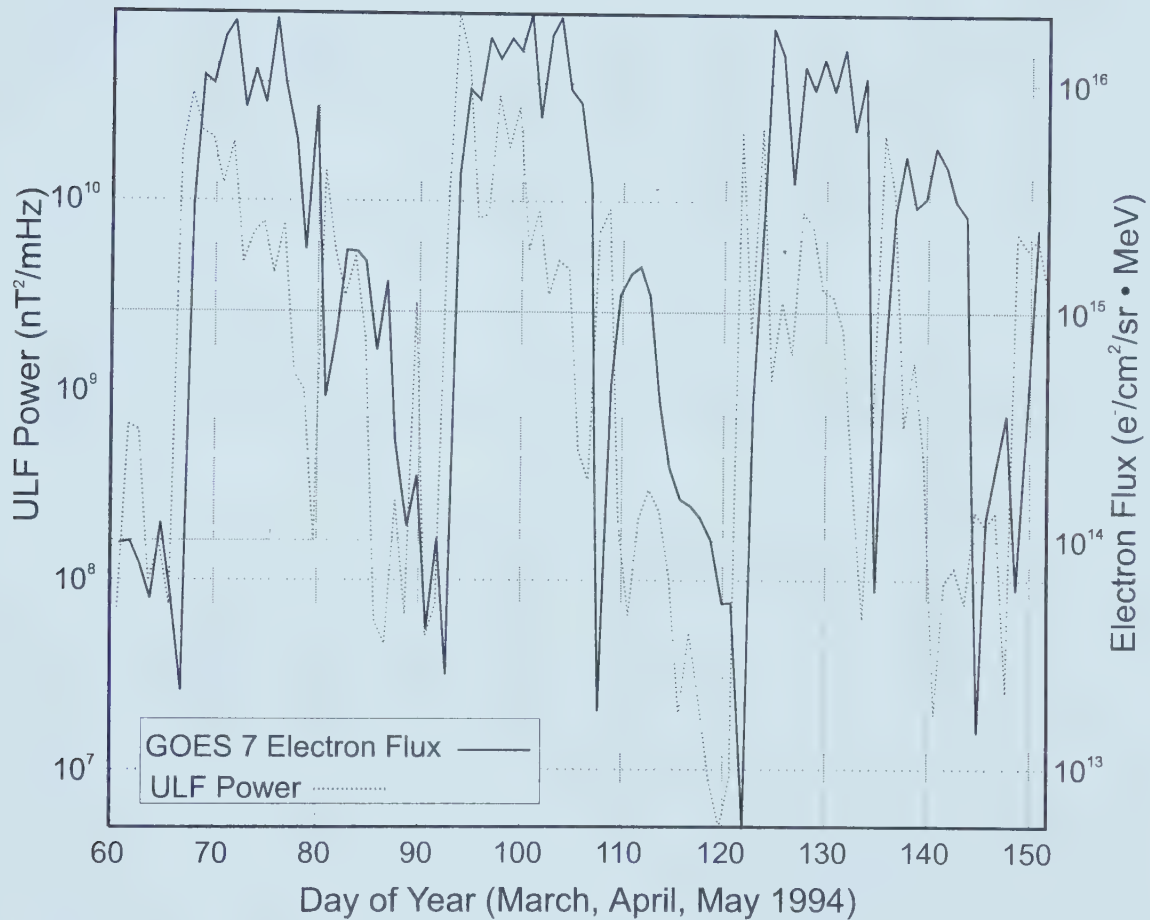


Figure 2.7 Energetic electron fluxes ($E > 2$ MeV) (drawn in the solid line) measured near geostationary orbit by GOES 7 and power in the ground based magnetometer data in the ULF frequency band (drawn in the dotted line) during a period of 92 days in 1994 at Gillam, MB. Gillam and GOES 7 are approximately in the same time zone.

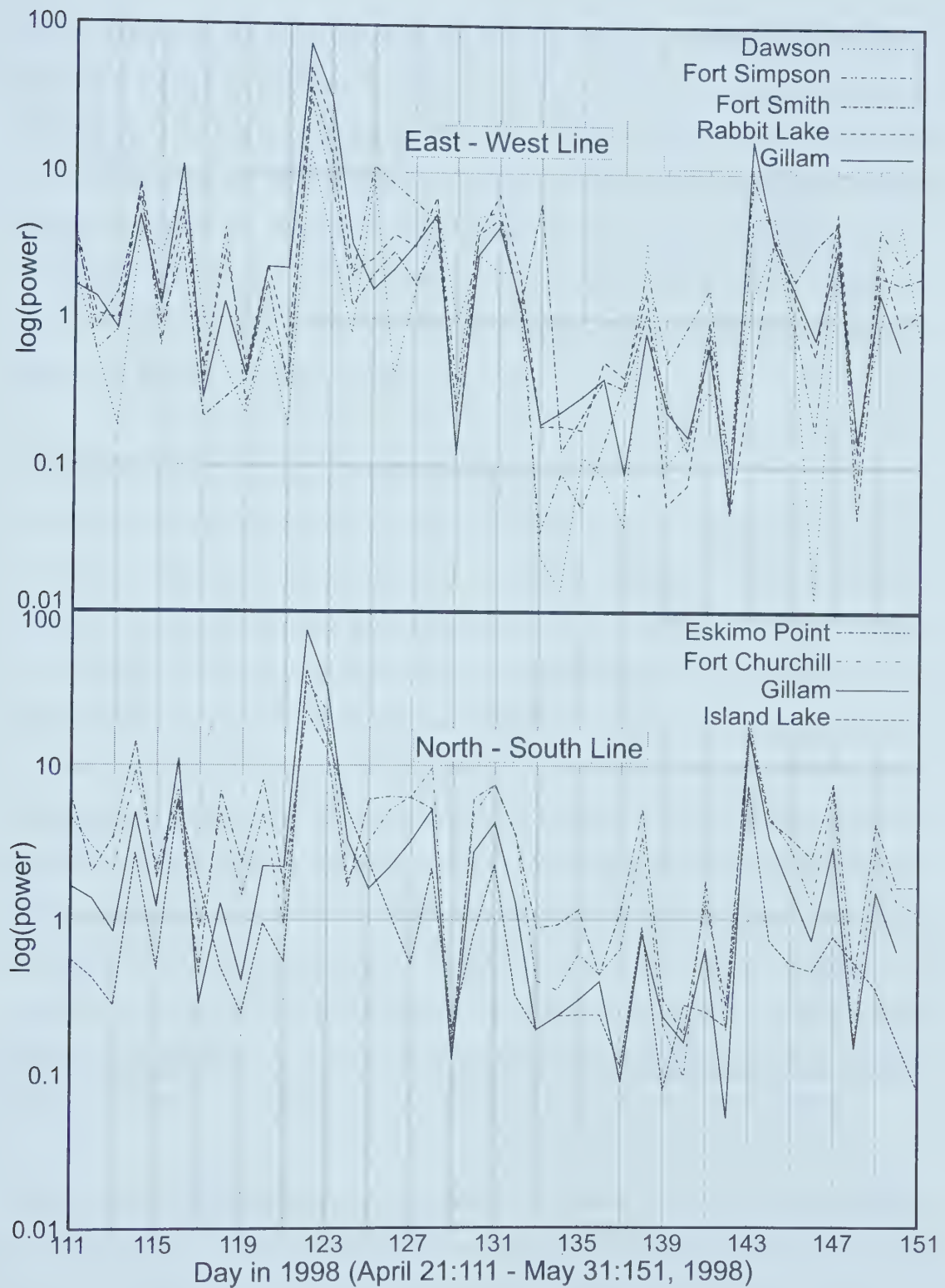


Figure 2.8 Power in ULF pulsations (in the 0.8 - 20 mHz range) showing the longitudinal and latitudinal extent of the pulsations from April 21 (day 111) to May 31 (day 151) of 1998

Another possibility for the source of the ULF pulsations is global magnetospheric oscillations caused by pressure variations of the solar wind. The solar wind pressure variations cause the magnetopause to oscillate which creates global compressional waves within the magnetosphere that also can couple into shear Alfvén waves which can be observed on the ground. A theoretical mechanism for global magnetospheric oscillations producing relativistic electrons is discussed in section 2.6 below while a theoretical mechanism for the shear Alfvén wave component to produce relativistic electrons is discussed in section 2.5 which follows.

2.5 The Toroidal-Mode Oscillation Model

A toroidal-mode field line resonance in the ULF frequency range is proposed as a source of electron energization by *Elkington et al.* [1999]. Figure 2.9 outlines the basic acceleration model as a statistical drift-resonance model. The arrows in the figure indicate the direction of the electric field experienced by the drifting electron. Orbiting electrons, when in resonance with the oscillating electric field, are accelerated by the electric field each time they arrive in the dawn and dusk sectors. The electron will be located at dawn, while the electric field is radially inwards and the electron is being transported radially outwards. Half a drift period later, when the electron is at dusk, the electron will experience a radially outward electric field while being transported inwards. Thus $\vec{E} \cdot \delta\vec{r}$ is consistently negative, causing a potential drop. The interaction of an equatorially mirroring electron with toroidal mode ULF waves in this manner can cause an acceleration of the electrons. The rate of energization depends linearly on the magnitude of the dawn-dusk convection electric field as shown by *Elkington et al.* [1999].

It may be thought that only those electrons near the resonance frequency will be energized but *Elkington et al.* [1999] show that in the presence of the convection electric field, electrons below the resonance energy are energized in a stable attractor manner. This also shows that electrons may be accelerated in bulk using the toroidal resonance

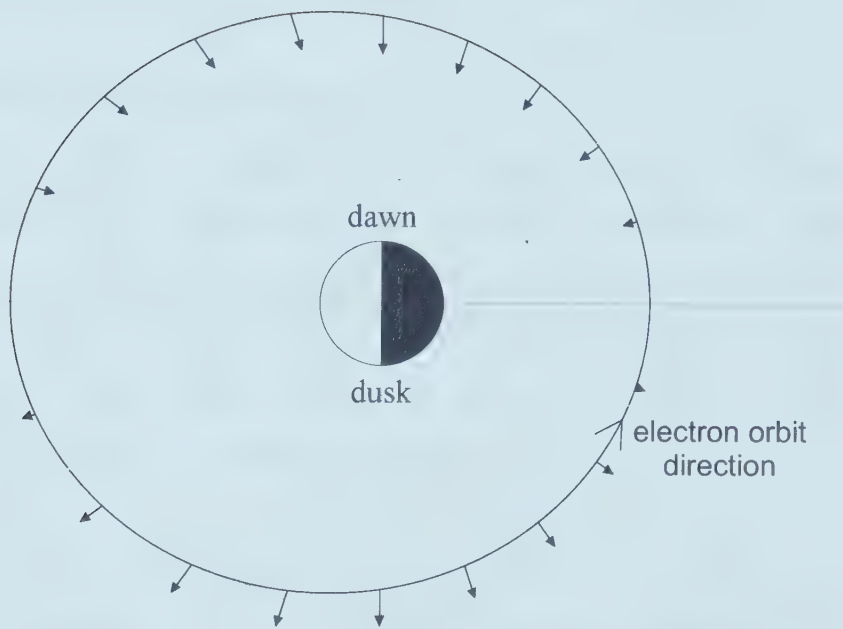


Figure 2.9 The toroidal-mode oscillation model. The solid arrows indicate the direction and magnitude of the radial electric field when the electron is at the location of the foot of the arrow. The open arrow indicates the direction of electron drift. Starting at dusk, the electron experiences a positive (radially outward) electric field and is transported radially earthwards and half a drift period later, the electron arrives at dawn, the electric field has become negative (radially inward) and causes the electron to be transported outwards. (Figure adapted from *Elkington et al.*, 1999.)

waves. The typical convection electric field values used are about 3-5 mV/m with a wave amplitude of about 3 mV/m. The radial oscillation used in the model is about $0.3 R_E$ and the toroidal electric field oscillates at about 3-5 mHz. Using these parameters, the electron energy, which starts at about 1.6 MeV, approximately doubles to triples in energy over about 10 hours. When the electrons begin with an energy of about 2.5 MeV, they gain about one order of magnitude in energy over the same time period.

2.6 The Compressional Wave Model

Radial transport is a slow process compared to the time scales required for the electron fluxes of energies above 2 MeV to rise by an order of magnitude. The time for a particle to diffuse radially from about 8 to $6.6 R_E$ is about 10 hours [Baker *et al.*, 1989; Liu *et al.*, 1999]. Liu *et al.* [1999] describe a process of “magnetic pumping” which uses magnetohydrodynamic (MHD) waves to increase the speed of the energization process over the required time scales of hours rather than days.

The basic compressional wave model (Figure 2.10) uses MHD waves to move the Earth’s magnetic field lines toward the Earth and outwards again and uses pitch angle scattering to break the process reversibility. The pitch angle scattering required in this mechanism does not need to bring the pitch angle of the particle near the loss cone and occurs every several minutes rather than days. Since the pitch angle of the electrons can be increased or decreased, the energy of the electron can increase or decrease.

The calculations by Liu *et al.* [1995] simulate the energization of ions and are here applied to electrons. Let us consider one MHD cycle beginning with an electron on an outer field line with a pitch angle of 0° and an initial energy of E_i . Since the pitch angle begins at 0° , the first adiabatic invariant is identically zero and we only need to conserve the second adiabatic invariant. The outer magnetic field line is longer than the inner magnetic field line ($\ell_{outer} > \ell_{inner}$) and thus at the end of the first part of the cycle, after the MHD wave has moved the magnetic field lines towards the Earth, there is an energy gain.

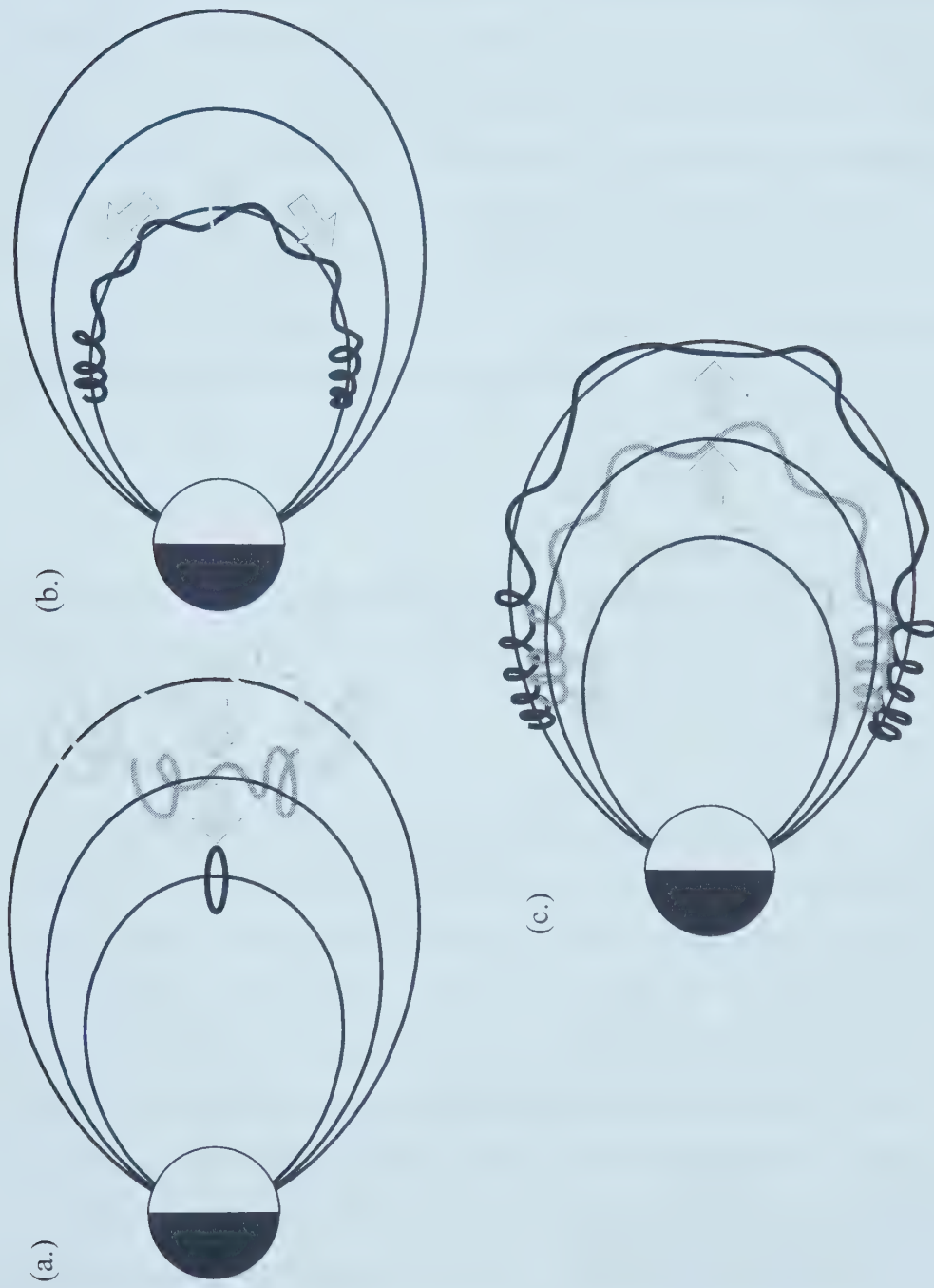


Figure 2.10 The compressional wave model. (a.) Radial diffusion: conserving the first and second adiabatic invariants with energy gain; (b.) Pitch angle scattering: conserving energy while remaining on the same magnetic field line; (c.) Radial diffusion: conserving the first and second adiabatic invariants with an energy loss. (Figure adapted from Fujimoto *et al.*, 1990a.)

The electron then undergoes pitch angle scattering: $\alpha=0^\circ \rightarrow \alpha=90^\circ$ with no appreciable energy change. Finally the MHD wave drives the magnetic field lines back outwards but this time the second adiabatic invariant is identically zero and the first invariant is conserved with an energy loss. The first part of the cycle shows a net energy gain $E_f = E_i \times \lambda$ with $\lambda > 1$. Similarly if we started with a pitch angle of 90° and ended with a pitch angle of 0° , the electron would experience first an energy gain then an energy loss with a net energy loss $E_f = E_i / \lambda$ again with $\lambda > 1$. Thus, averaging both extremes to achieve a more appropriate picture of the real final electron energy: $E_f = E_i \times \frac{1}{2\lambda} + E_i \times \frac{\lambda}{2}$. By doing a Taylor expansion (with $\lambda = 1 + \varepsilon$, and $\varepsilon \ll 1$), we can see that the electron experiences a second order energy gain as follows:

$$\overline{\Delta E} = E_f - E_i = \frac{\varepsilon^2}{2} E_i$$

The fact that we have a zero energy barrier (a particle cannot lose an infinite amount of energy) means that there will be statistically a net energy gain over time.

2.7 Thesis Direction

In the four year survey of relativistic electron events and solar wind data, we noted a high degree of solar wind speed variability during times of electron energization. The solar wind ion density was noted to rise and be highly variable near the time of electron energization events as well. These facts suggested that the solar wind pressure fluctuations in the ULF range might excite compressional wave activity, that being a critical component of the compressional wave model proposed by *Liu et al.* [1999]. This however, of course does not rule out the toroidal-mode oscillation model proposed by *Elkington et al.* [1999] since the same compressional waves can produce the global toroidal oscillations which their model uses. We examine the possibility that the solar wind dynamic pressure oscillations in the ULF range might provide the MHD waves of the compressional wave model proposed by *Liu et al.* [1999] by looking at the solar wind data and geostationary near relativistic electron observations during the interval from

data and geostationary near relativistic electron observations during the interval from January 1995 to December 1998. The question this thesis is trying to answer is “might the solar wind pressure variations in the ULF range play a role in the energization of electrons near geostationary orbit?”

Chapter 3

Instrumentation and Data Analysis

3.1 Electron Near Geostationary Orbit

3.1.1 GOES

Among many satellites in space, the Geostationary Operational Environmental Satellites (GOES) provide the weather pictures seen daily on television and carry many monitoring instruments as discussed below. The GOES satellites are in *geostationary orbit*, meaning that these satellites orbit the earth equatorially at $6.61 R_E$ and complete one orbit in the same time as the earth itself takes to complete one rotation; thus these satellites remain continuously over one fixed point of Earth. There have been many GOES satellites launched over the past two decades. NASA launched the first GOES satellite for the National Oceanic and Atmospheric Administration (NOAA) on October 16, 1975 and followed it with another in June 16, 1977. Currently, NOAA is operating GOES-8 and GOES-10 for the purposes of atmospheric and space weather monitoring. The GOES satellites used in this study are GOES 7, 8 and 9/10 and are located, when in operation, at the easterly position of $75^\circ W$ or at the westerly position of $135^\circ W$ to provide a full view of the western hemisphere. Table 3.1 shows the longitudinal positions and times of local noon for the later GOES satellites. The initial series of satellites were *spin stabilized* and beginning with GOES 8 the basic platform design was changed to one called *3-axis* or *body stabilized*.

Satellite	Launch Date	Date Activated	Longitude	Local Noon	Failure Date
GOES 7	Feb. 26, 1987	Mar. 25, 1987	$112^\circ W$	19:28	Jan. 1996
GOES 8	Apr. 13, 1994	June 9, 1995	$75^\circ W$	17:00	—
GOES 9	May 23, 1995	Jan. 25, 1996	$135^\circ W$	21:00	Jul. 27, 1998
GOES 10	Apr. 25, 1997	Aug. 1998	$135^\circ W$	21:00	—

Table 3.1. GOES satellite positions and time of local noon

In addition to the atmospheric weather monitoring which the GOES satellites are designed to do, they also carry a series of space weather monitoring instruments (Figure 3.1). The three main components of space weather monitored by GOES are X-rays, energetic particles, and magnetic field via the Space Environment Monitor (SEM) system. In this thesis we deal with data from the energetic particle sensor.

3.1.2 The GOES Energetic Particle Sensor

The EPS unit, located on the easterly facing panel of the satellite, consists of a telescope subassembly, a dome subassembly and signal analyzer unit/data processing unit (SAU/DPU); the latter unit provides the final amplification of the telescope and dome output signals. These components are mounted next to the solar array on the spacecraft's south equipment panel within the spacecraft main body, and view the space environment through apertures. The EPS performs three integral measurements of electrons from 0.55 to more than 4.0 MeV on the dome. These data are given in units of counts/cm²/s/sr.

The dome (Figure 3.2) employs three sets of two 1.5 mm thick, 25 mm², silicon surface barrier detectors (SSBD), each with different thickness moderators covering its field of view, thus providing three different energy thresholds. In the SSBD, the energy lost by ionizing radiation (protons, alpha particles or electrons) ultimately results in the creation of electron-hole pairs which are collected by an electric field. By using electrical contacts that are placed in the SSBD, a current proportional to the ionization can be detected. This current can then be converted to a collection of electric pulses for analysis. These electric pulses are passed through preamplifiers, converting them into voltage pulses before being routed to the SAU/DPU. The dome has a 2 steradian field of view (57.3° cone) with an accumulation sampling rate of once every 10.2 or 20.5 s and the data is then 5 minute averaged. For the initial series of GOES satellites, due to the spin-stabilization (0.6 second rotation rate) and the relatively long accumulation time (>10s), the data are spin-averaged. The three electron integral bands (E1, E2 and E3) have thresholds of 0.55, 2 and 4 MeV respectively [NASA, 1996].

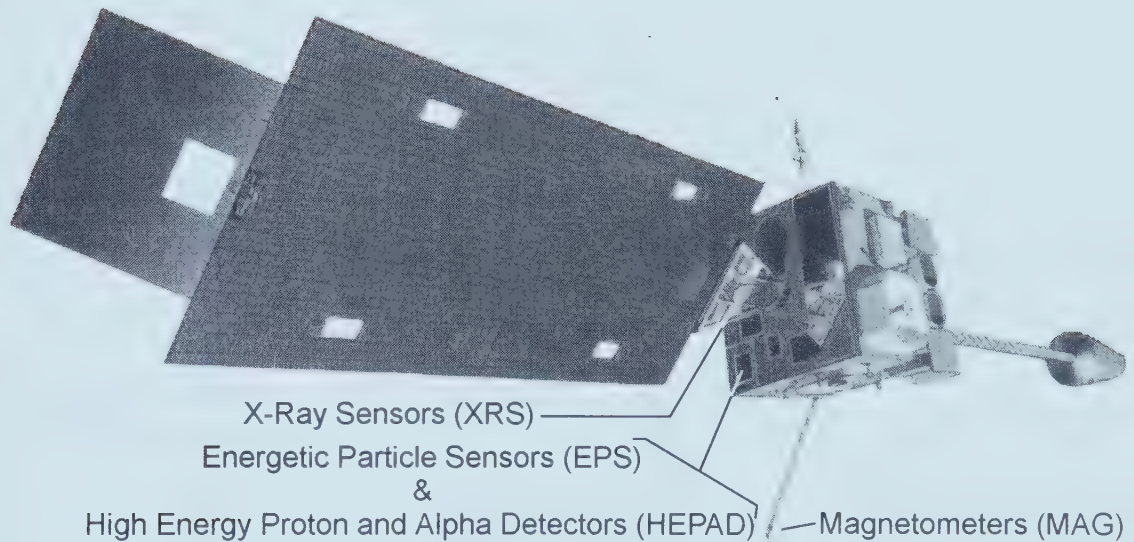


Figure 3.1 The GOES satellite showing the south panel (to which the solar array is attached) bearing the HEPAD panel which contains the energetic particle sensors and the high energy proton and alpha detectors as part of the space environment monitor system instruments. (Figure adapted from *NASA*, 1996.)

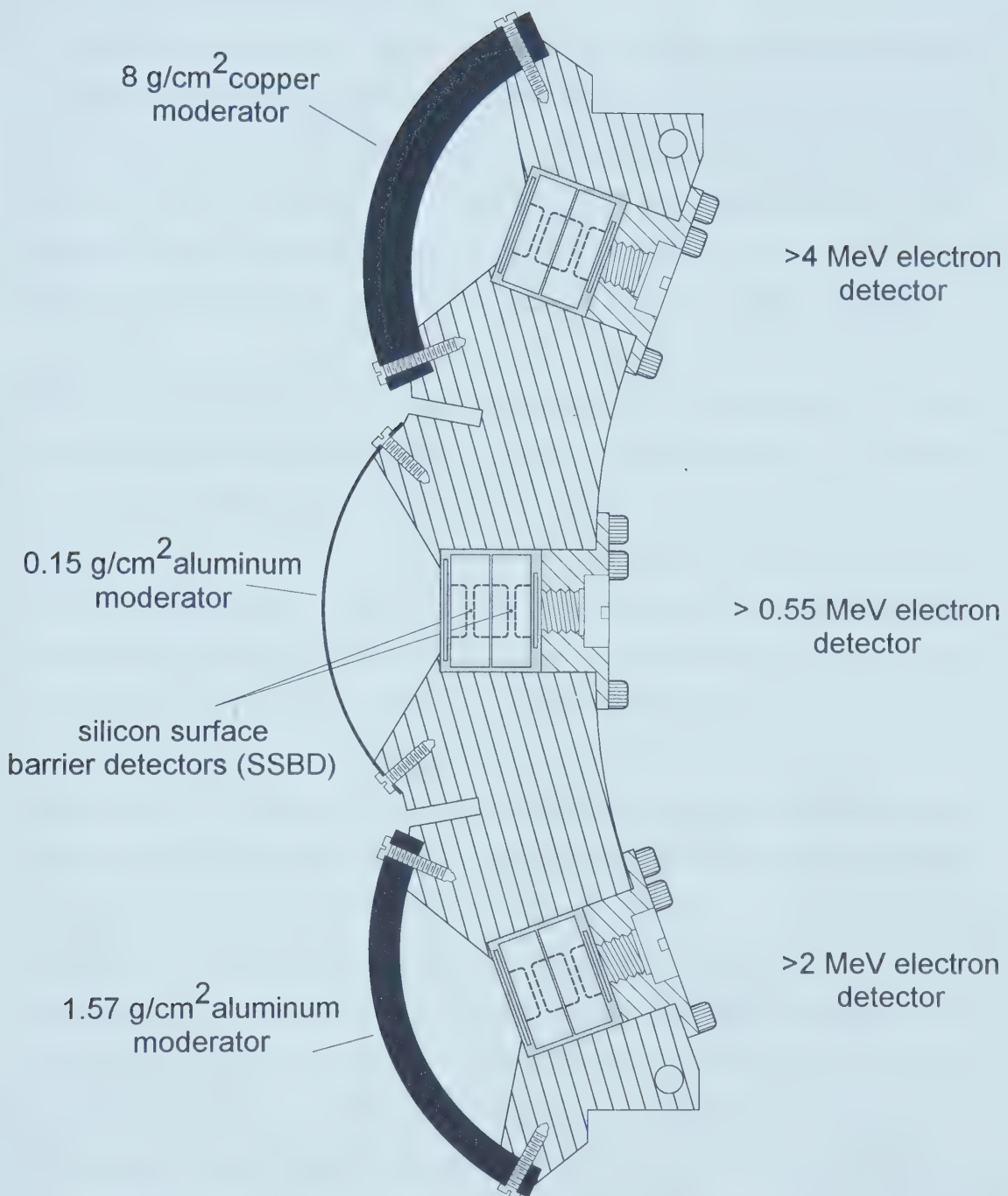


Figure 3.2 The dome subassembly of the energetic particle sensor (EPS) on the GOES satellites. The three energy ranges (>0.55 , >2.0 and >4.0 MeV) are detected by three separate pairs of silicon surface barrier detectors and moderated by aluminum and copper of varying thicknesses. The dome subassembly is mounted on the HEPAD/EPS panel.

3.1.3 GOES Electron Data

The electron data used in this study are 5-minute averaged integrated electron flux ($E > 2$ MeV) measured in units of electrons/cm²/s/sr. These units of energetic electron fluxes were changed to electrons/cm²/sec/sr • MeV (matching the other channels of particle measurements on the GOES satellites and following *Rostoker et al.* [1998]), resulting in only a vertical shift on the plots of the log of fluxes. We only use the local maximum in the electron flux near the time of local noon of the GOES satellite.

Near geostationary orbit, the energetic electron fluxes ($E > 2$ MeV) can rise very rapidly and remain elevated for periods of days to weeks many times each year. The observed time for the energetic electron fluxes to be enhanced to relativistic energies near geostationary orbit is typically about 8-10 hours. A plot of the energetic electron fluxes for May 1998 is shown in Figure 1.8. The top bounding line shows the maximum electron flux points for each day near local noon. There are several features to note in this example which are common to most electron energization events. First that the electrons drop out for a short period of time before there is a very large increase in electron fluxes. This drop out is due to the fact that during a geomagnetic storm the magnetosphere is highly disturbed and the third adiabatic invariant is no longer conserved. The electrons are likely being energised throughout this period of low electron fluxes but the particle orbits around the Earth are open and the electrons are lost on their orbit to the night side of the magnetosphere to the plasma sheet. Secondly, during the recovery phase of the geomagnetic storm the magnetosphere is relaxing from its disturbed configuration and the electron flux rises *very* quickly — over a time span of a few hours (8-10 hours). The electrons are energised over a broad L-shell range between the magnetopause (about $L = 10$) and the average position of the outer edge of the outer radiation belt (about $L = 5$) as shown by *Rostoker et al.* [1998].

Further examples of electron events are discussed in a later section.

3.2 Variations of the Solar Wind

3.2.1 WIND Satellite

While many aspects of the solar wind can be studied by Earth orbiting satellites, to draw a clearer picture of the solar wind and its interaction with the magnetosphere, NASA launched the WIND satellite on November 1, 1994 (Figure 3.3a). The WIND spacecraft carries a set of eight scientific instruments for measuring the density and speed of charged particles and electric and magnetic fields that characterize the solar wind. WIND, together with Geotail, Polar, SOHO, and Cluster projects, make up a cooperative scientific satellite project named the International Solar Terrestrial Physics (ISTP) program. WIND is spin stabilized at 3 seconds/rotation around an axis perpendicular to the ecliptic. For most of the period of this study, WIND was orbiting the Earth with an orbit that extended about $250 R_E$ sunward and was in a small “halo” orbit, about the sunward Sun-Earth gravitational equilibrium point (L1), varying from 235 to 265 Earth radii. Therefore the satellite provides nearly continuous monitoring of the solar wind conditions near Earth orbit.

The instrument used in this study is the Solar Wind Experiment (SWE) instrument, consisting of five integrated sensor/electronics boxes and a data processing unit (DPU). The sensor units are mounted on the top and bottom shelves of the spacecraft facing radially opposite directions, 15° above and below the equatorial plane (Figure 3.3b). The ion density, temperature and velocity of the solar wind, particles with energies ranging from 7 eV to 24.8 keV, are measured by a pair of 20 cm in diameter Faraday Cup analyzers. The proton velocity is determined in the range of 200 - 1250 km/s with about 3% accuracy and the proton number density in the range of 0.1 - 200 protons/cm³ with about 10% accuracy [Ogilvie *et al.* 1995].

For a full description of all WIND instrumentation, the reader is referred to the reviews in *Russell* [1995].

(a.)

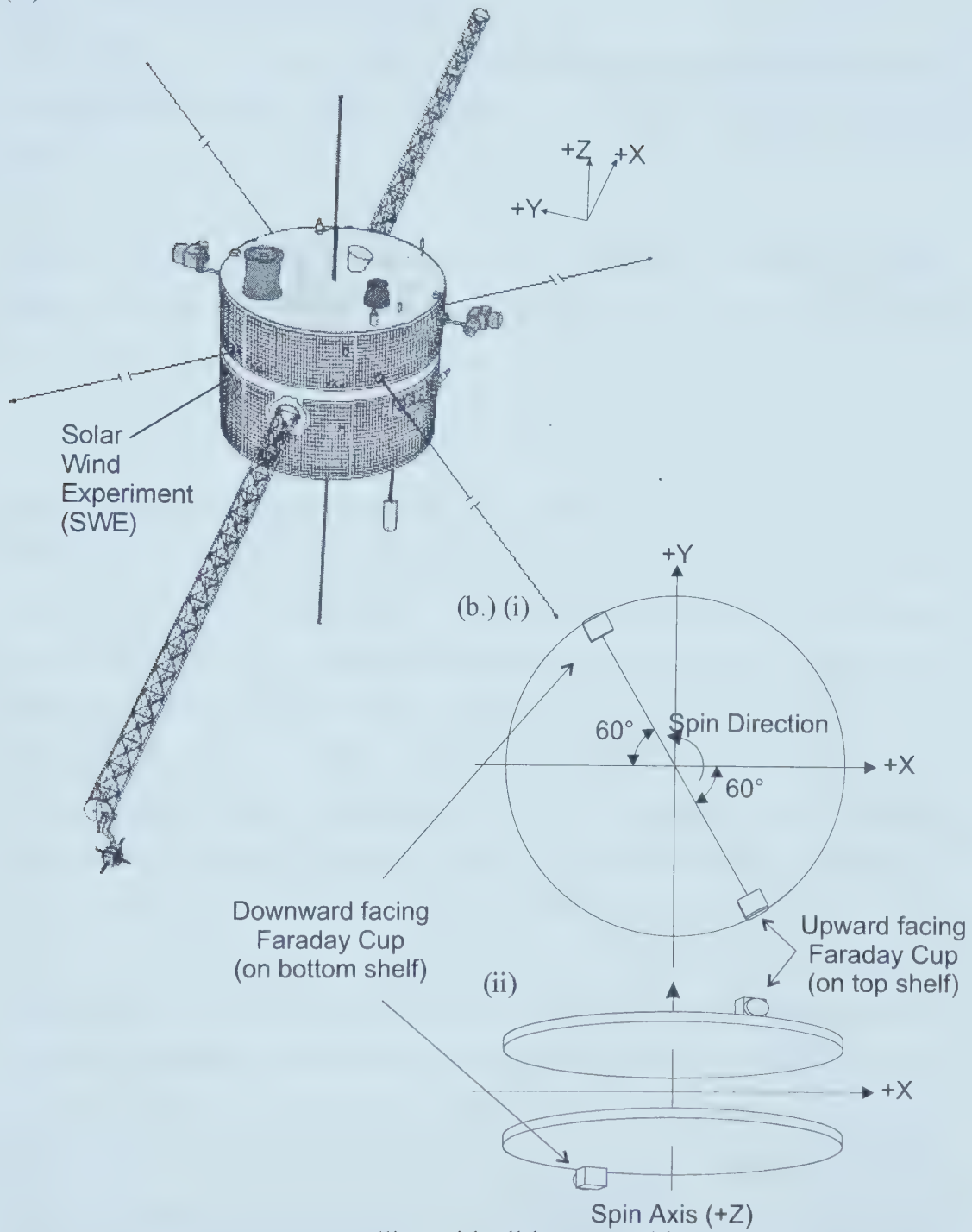


Figure 3.3 (a.) The WIND satellite, with all booms and instruments as deployed in space, showing the location of the solar wind experiment. The axis of rotation is vertical ($+Z$) in this diagram. At the indicated location, the Faraday Cup aims 15° below the equatorial plane and on the radially opposite side a second Faraday Cup aims 15° above the equatorial plane. (b.) WIND schematic showing the locations of the two Faraday Cups looking from the $+Z$ shown in (i) and the looking from the $-Y$ directions shown in (ii) (Figures adapted from Ogilvie *et al.*, 1995.)

3.2.2 Presentation of WIND Data

In this study, we use the solar wind particle density data and the solar wind speed data as measured by the WIND satellite. These data are measured with a 90 second sampling rate.

The solar wind proton density (n , measured in protons/cm³), the proton mass (m_p) and the speed of the solar wind toward the Earth (v_x , measured in km/s) are used in calculating the solar wind dynamic pressure (P , measured in nPa):

$$P = m_p n v_x^2$$

Since the data are measured by WIND at a sample rate of one data point every 90 seconds, there are therefore 40 data points in a one hour period. Since the fast Fourier transform (FFT) requires 2^n data points, where n is a positive integer, 64 ($= 2^6$) points are needed for the FFT. After making this time series into a vector with 64 points by zero padding, the gaps in the WIND data, as well as the last 24 points, are filled with the closest previous valid value. If there was a data gap at the start of the data, the first valid point was extended back to the beginning of the data, filling the gap. The DC value was then removed by setting the last point to zero and shifting all points accordingly. The FFT is taken of this entire 64 point time series. After being band passed in frequency space for the 1-5.5 mHz frequency range using a step filter, the power spectrum is calculated on an hourly basis. The time periods in which there are WIND data gaps are not used in comparisons with the electron energization data. The solar wind pressure power is calculated to be typically in the range of $10^{13} - 10^{15}$ nPa²/mHz but rises to over 10^{16} nPa²/mHz at times and falls to 10^{10} nPa²/mHz on occasion. In cursory studies of the solar wind dynamic pressure and electron energization events, it was determined that approximately every time that the dynamic solar wind pressure power rose to about 5×10^{14} nPa²/mHz, we also observed an electron energization event. Thus we chose to investigate only those solar wind pressure events with more power than 10^{14} nPa²/mHz. Two sample days are shown in Figure 3.4 and Figure 3.5 which are discussed below.

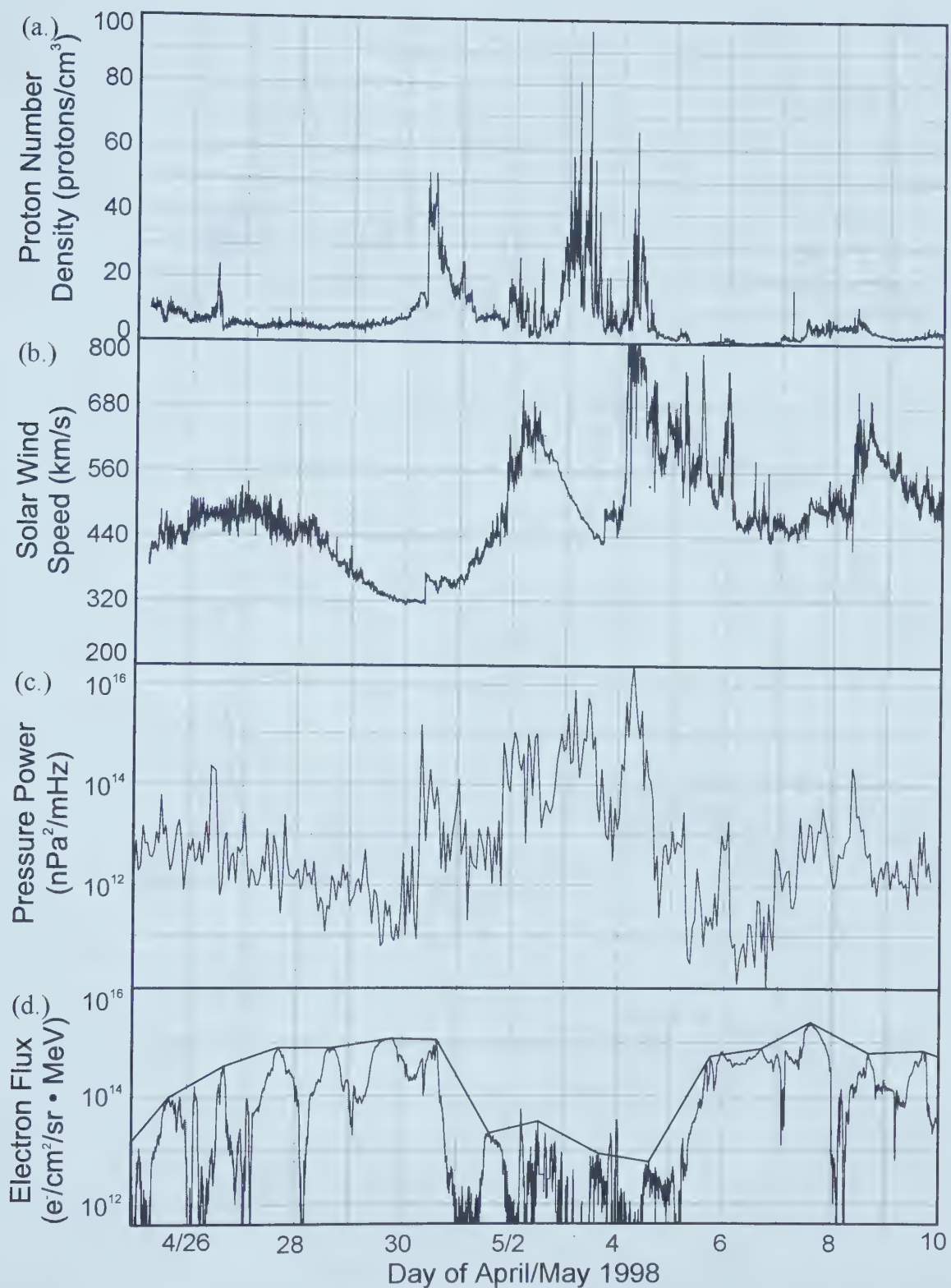


Figure 3.4 Space conditions during the period of April 25 to May 10 of 1998. (a.) Solar wind proton number density, (b.) Solar wind speed; (c.) Hourly solar wind pressure power in the Pc 5 band. (d.) Energetic electron flux near geostationary orbit ($E > 2$) measured by GOES 8.

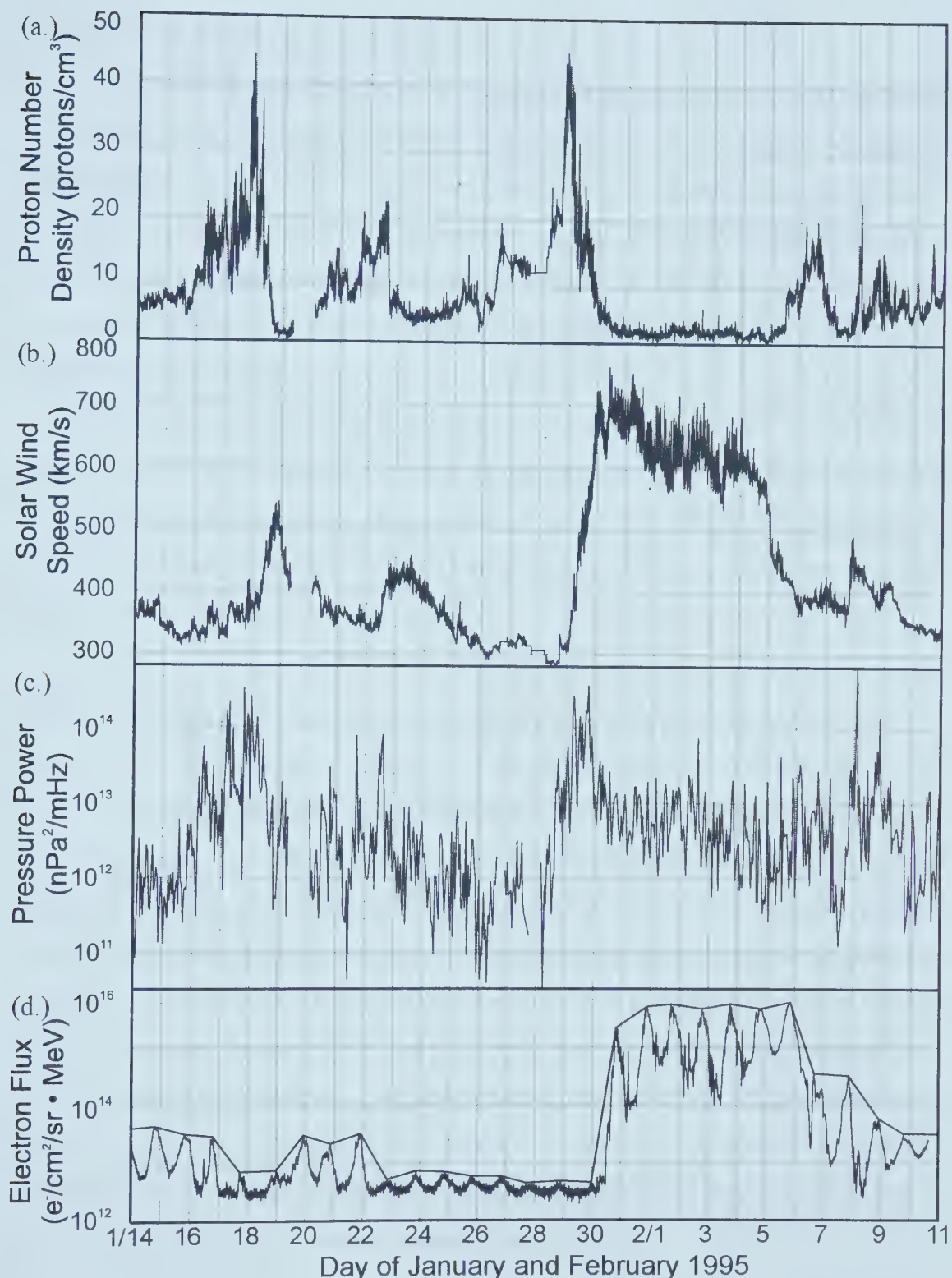


Figure 3.5 Space conditions for January 14 to February 11 of 1995. (a.) Solar wind proton number density; (b.) Solar wind speed; (c.) Hourly solar wind pressure power in the Pc 5 band. (d.) Energetic electron flux near geostationary orbit ($E > 2$) measured by GOES 7.

3.2.2.1 May 1998

Figure 3.4 shows the solar wind data as measured from April 25 to May 10 of 1998. First, within one day of May 4, we observed that the solar wind proton number density and the wind speed rose to their respective highest levels during the time period plotted. Secondly we also note that there is an immense amount of variability in both data sets. The third panel of Figure 3.4 shows the hourly pressure power of the solar wind in the Pc 5 range. The aforementioned variability is demonstrated by the peak in this power plot. The pressure power at the peak is 2.3×10^{16} nPa²/mHz. Throughout this event, we note that the solar wind velocity is observed to vary over a large range — the solar wind velocity is not relatively constant but rather varies from local minima to local maxima on the timescale of days. GOES 8 shows a sharp increase in the electron flux on May 5, 1998. This increase in electron flux follows the peak solar wind pressure power by about 18 hours.

3.2.2.2 January 1995

Figure 3.5 shows the solar wind data as measured from January 14 to February 11 of 1995. Late on January 28, we observe that the solar wind proton number density rises to a local maximum and that the wind speed rises to its local maximum in approximately the space of one day. Once again the hourly solar wind power in the Pc 5 range is plotted in the lower panel. This second event has a moderately high peak dynamic pressure power of 3.7×10^{14} nPa²/mHz and is associated with the rise in solar wind velocity. In this event we note that the solar wind changed from a relatively slow wind of between 300 - 400 km/s to 600 - 700 km/s. The peak dynamic pressure power occurred at around 18:00 UT on January 29, 1995 and the energetic electron flux, as measured by GOES 8, underwent a sharp increase on January 30 at around 12:00 UT — again about 18 hours after the peak solar wind dynamic pressure power.

3.3 Event Definitions

An *electron event*, for the purposes of this study, is defined as a period of time during which the energetic ($E > 2\text{MeV}$) electron flux rises more than one order of magnitude (irrespective of the absolute flux level) in two or fewer days. A *solar wind* event is defined as any hourly period when the solar wind pressure power exceeds $10^{14} \text{nPa}^2/\text{mHz}$ and if such an event occurs within three days of an electron energization event then it is considered to be associated with the electron energization event. Each *event date* referred to is the beginning of the event.

3.4 Solar Wind Statistics

The time periods involved in this study are January 1995 to December 1998. All valid WIND pressure (speed and proton number density) data are used in this study and compared to all valid electron flux data from GOES 7, 8 and 9/10. A sample of the data studied are shown in Figure 3.6 and the entire dataset, showing the Dst, WIND and the GOES data, may be found on the internet at <http://sikkema.netfirms.com/plots/plots.html>.

Over the four year period of our study, we found 990 time periods when the average solar wind pressure power in the ULF range exceeded $10^{14} \text{nPa}^2/\text{mHz}$ and 568 of these time periods have an associated electron energization event. Since there is a three day window prior to an electron energization event during which hourly solar wind events may occur, there are a far greater number of solar wind events associated with electron energization events than electron energization events themselves. Figure 3.7 shows the number of electron energization events associated with a given number of solar wind events within that 3-day window. In total, over the four years, there are 78 electron energization events and in Figure 3.8 we plot the percentage of the solar wind events within the specified pressure range associated with any of the 78 electron energization events. We expect that at low solar wind pressure powers, fewer solar wind events are associated with the electron events. Figure 3.8 shows a lower limit for a 1:1 correlation between the solar wind events and the electron events. For every time period when the solar wind dynamic

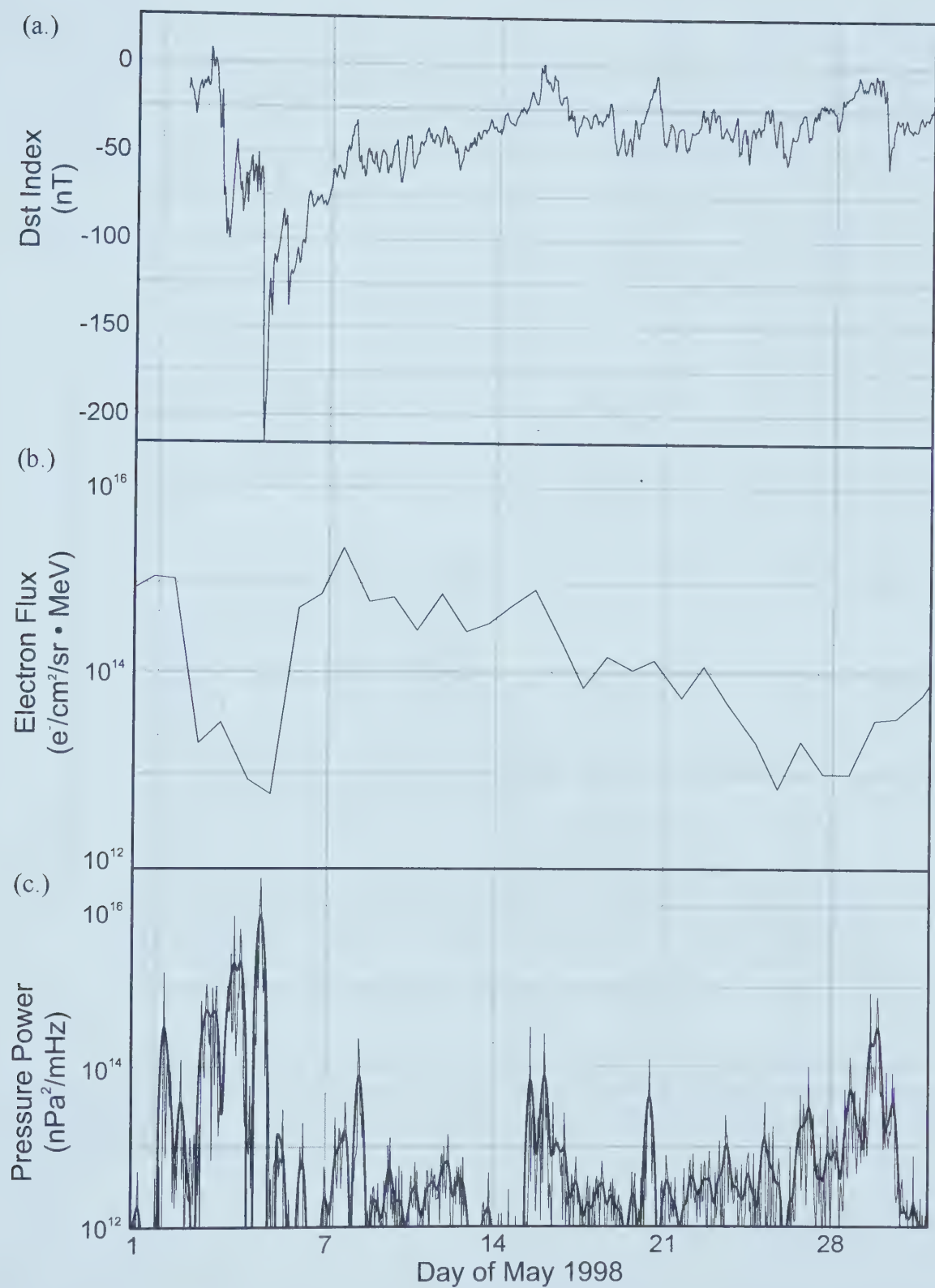


Figure 3.6 Space conditions for May 1998 (a.) Dst index (b.) energetic ($E > 2$ MeV) electron flux (measured by GOES 8) (c.) Solar wind dynamic pressure power actual data (thin black line) and smoothed data (thick black line) for visual analysis.

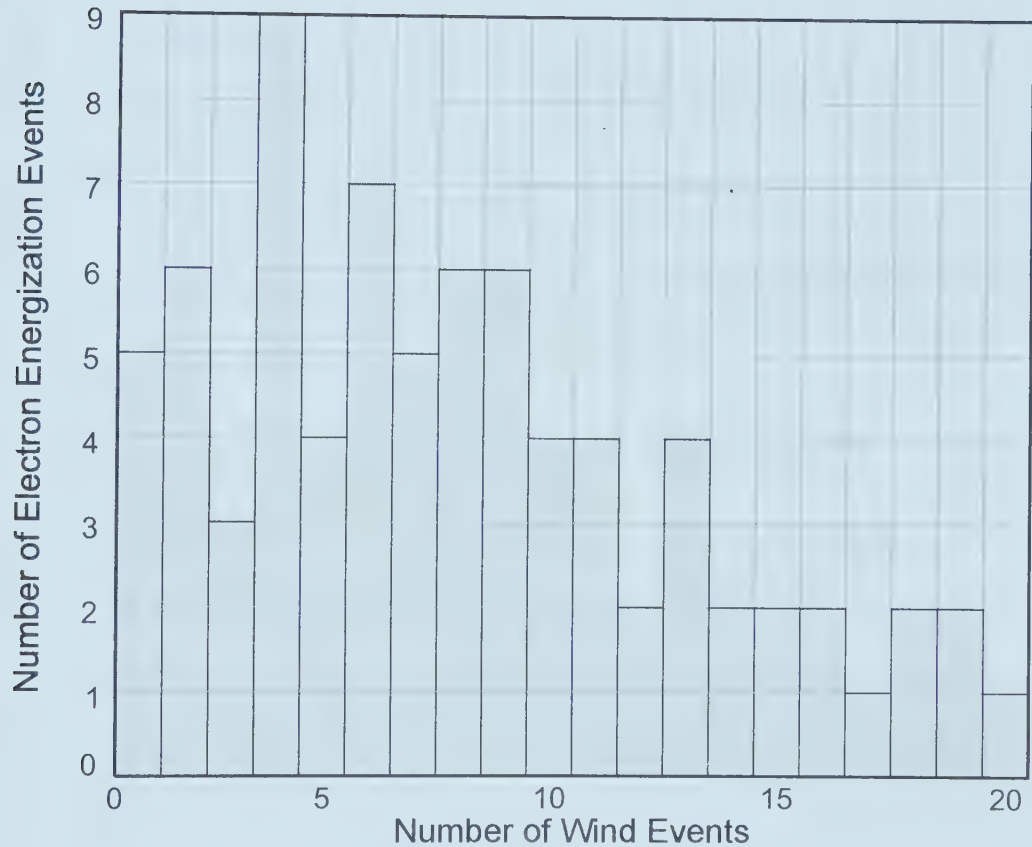


Figure 3.7 The number of electron energization events with the given number of solar wind events with more dynamic pressure power than $10^{14}\text{nPa}^2/\text{mHz}$ during the period of January 1995 - December 1998.

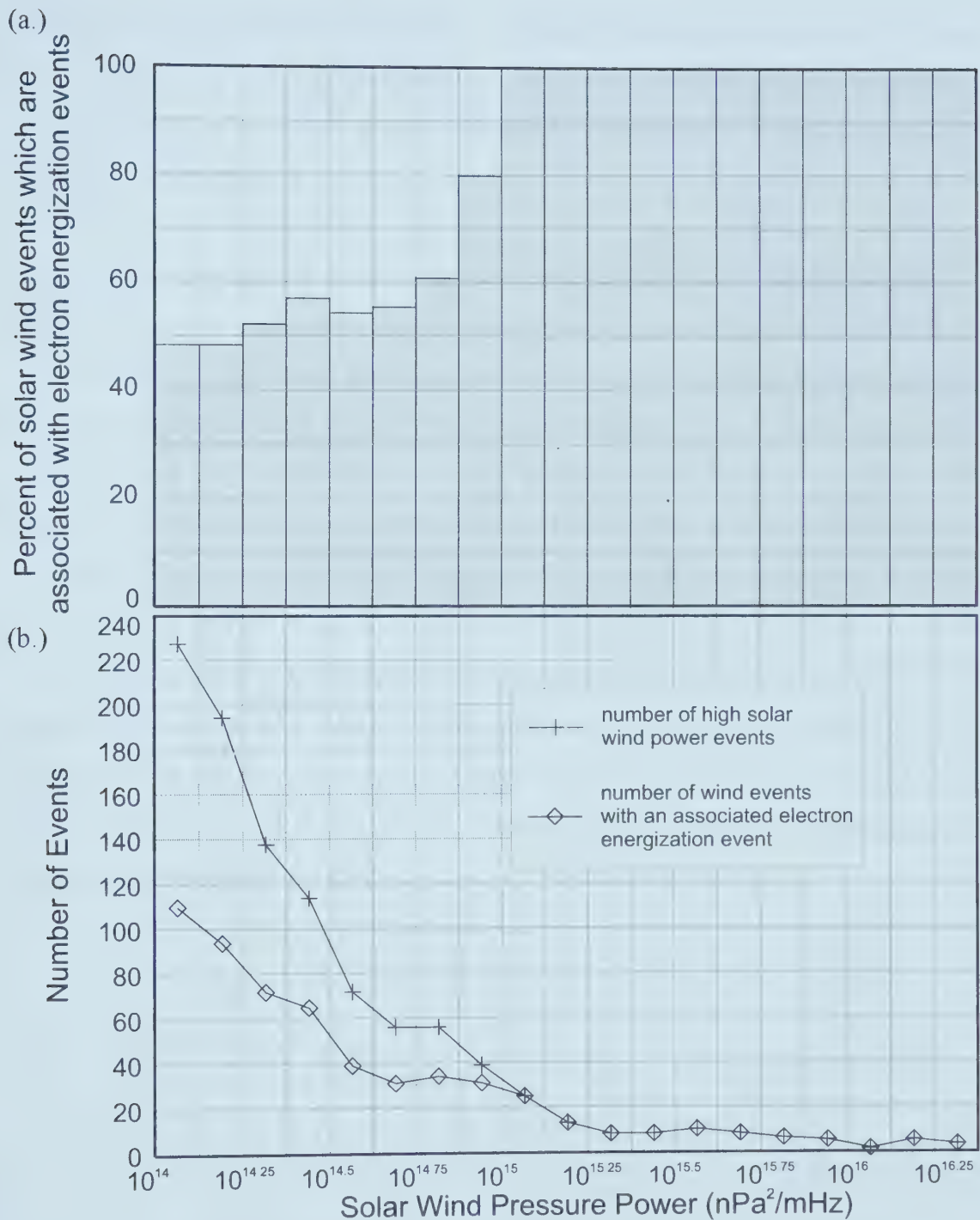


Figure 3.8 (a.) Percentage of solar wind time periods which are associated with electron energization events as a function of peak power in the Pc5 frequency band of solar wind pressure variations. The power is computed on hourly intervals of solar wind dynamic pressure over the four year period from January 1995 to December 1998. The electron energization events are identified as sharp increases in the >2 MeV electron flux as measured near geostationary altitudes by GOES 8. (b.) The number of events used in the calculations of the top panel.

pressure power exceeded 10^{15} nPa 2 /mHz, we always observed an associated electron energization event. This is an important result since we can predict, with great confidence, that an energization event will occur if we know that the pressure power exceeds 10^{15} nPa 2 /mHz.

In Figure 3.9a comparison is shown of the distribution of solar wind speeds using the 73 solar wind events which had a solar wind dynamic pressure power greater than 10^{15} nPa 2 /mHz, which were also associated with one of the 29 high pressure power electron energization events (Figure 3.9a) to the distribution of solar wind speeds using all 29,838 hours for which there were data available during the entire study period (Figure 3.9b). We observe that both histograms in Figure 3.9 are approximately Gaussian in form. We also observe that, when the solar wind pressure power exceeds 10^{15} nPa 2 /mHz, energetic electron enhancements can occur over a wide range of solar wind speeds and not only for high speed winds. These facts indicate that solar wind pressure variations can be a source of global compressional waves in the magnetosphere independent of the KHI since the KHI would require a high speed solar wind flow [Wolfe *et al.* 1980] and these pressure variations may be more closely related to the appearance of energetic electrons.

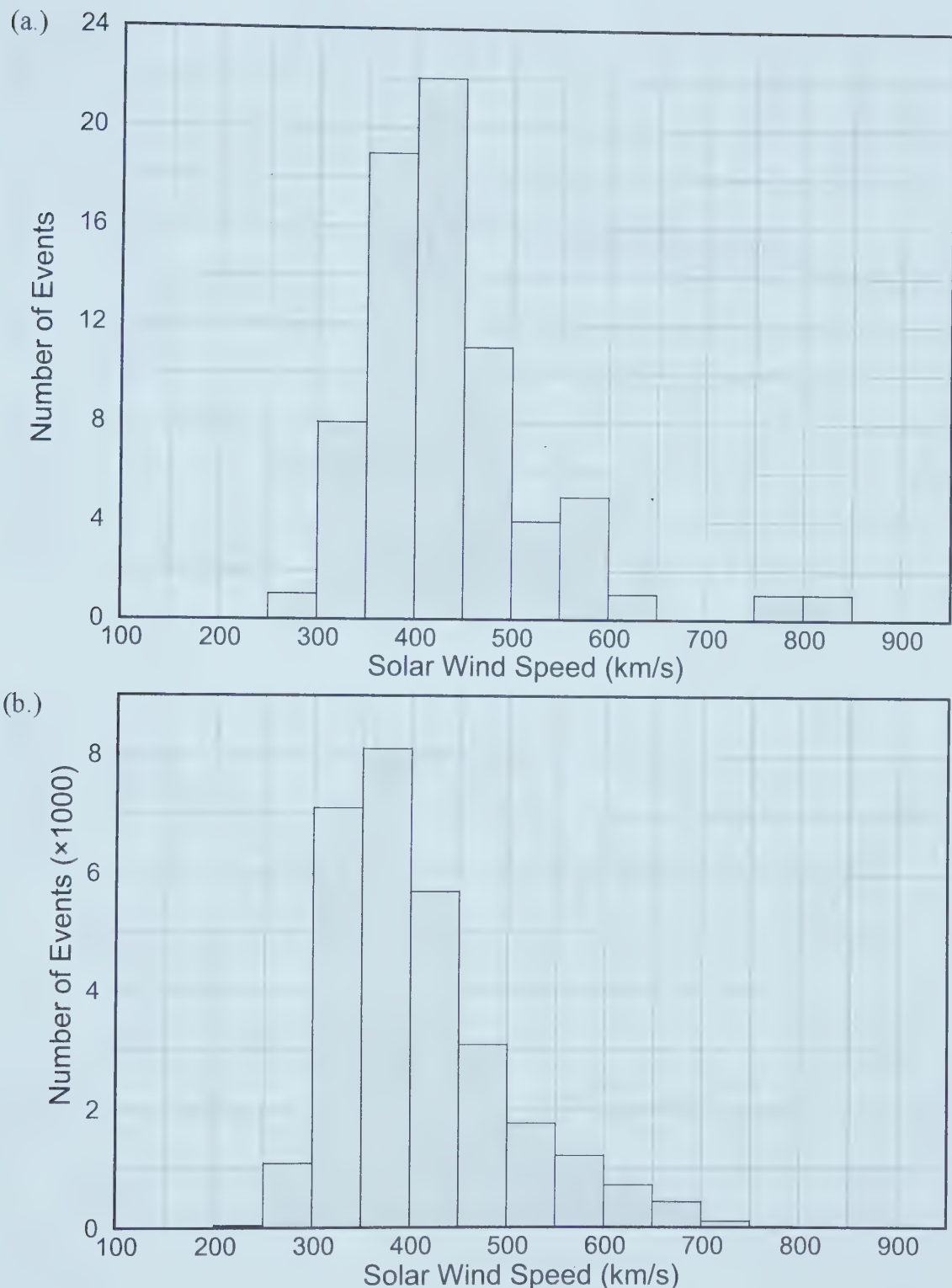


Figure 3.9 (a.) Distribution of solar wind speeds during an electron energization event during which the pressure power in the ULF band exceeded $10^{15} \text{nPa}^2/\text{mHz}$
 (b.) Distribution of all solar wind speed data during the study time period of January 1995 - December 1998.

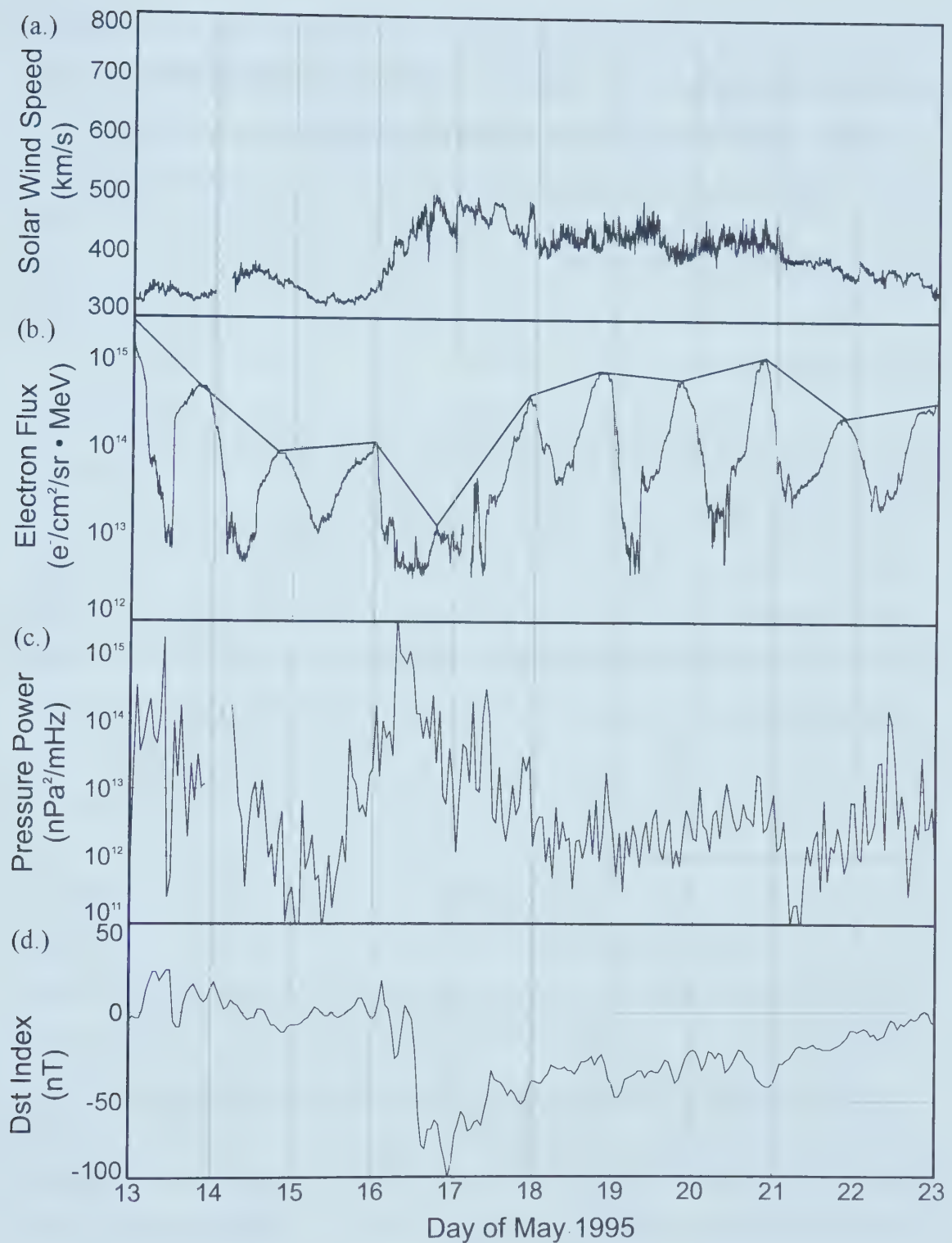


Figure 4.1 Space environment for May 13 to 23 of 1995. (a.) the low solar wind speed; (b.) the electron fluxes rising by nearly two orders of magnitude beginning on May 16; (c.) the dynamic solar wind pressure power which exceeded 10^{15} nPa^2/mHz on May 16 and (d.) the Dst index for this time period for reference.

Contrasting this figure with Figure 3.4 and Figure 3.5, we see that in this event the peak solar wind speed was below 500 km/s whereas the peak solar wind speed is around 700-750 km/s during many other electron energization events. The wind speed, as shown in this figure only began to rise less than one day prior to the rise in energetic electron fluxes. The solar wind dynamic pressure power, however, peaked on May 16 at 07:00 UT and the electron fluxes begin to rise later the same day. This demonstrates that high solar wind speeds and KHI are not necessary for electron energization to occur.

4.1.2 High ULF Power with No Electron Enhancement

Enhanced power in the ULF frequency band has been under scrutiny as a possible cause of the sharp rise in relativistic electron fluxes. As is shown in Figure 2.7, *Rostoker et al.* [1998] demonstrated, though do they not establish a causal relationship, that the power in the ground based magnetometer data in the ULF frequency range is enhanced prior to the sharp enhancement of electron fluxes near geostationary orbit. They go on to suggest that significant increases in fluxes of near-relativistic electrons near geostationary orbit are associated with enhanced power in the ULF frequency band in the morning hours.

The month of June 1996 was an exceptionally quiet time (there was very little variation in wind speed and the electron fluxes were down to almost the background level) in the near Earth region. Figure 4.2 shows the space conditions as measured by GOES, WIND and CANOPUS. The fact that there is very little variation in the solar wind speed is evidenced by the very low solar wind dynamic pressure power which peaks several times at about 8×10^{13} nPa²/mHz. The solar wind speeds are also relatively low making the KHI unlikely. In the lower panel, it can be seen that the power in the ULF frequency band was enhanced by about 1.5 orders of magnitude above the average quiet day power and yet no change is seen in the energetic electron fluxes. The enhanced ULF power does not appear to be due to either a KHI nor due to the solar wind pressure variations. This example does not rule out the connection between the enhancements of power in the

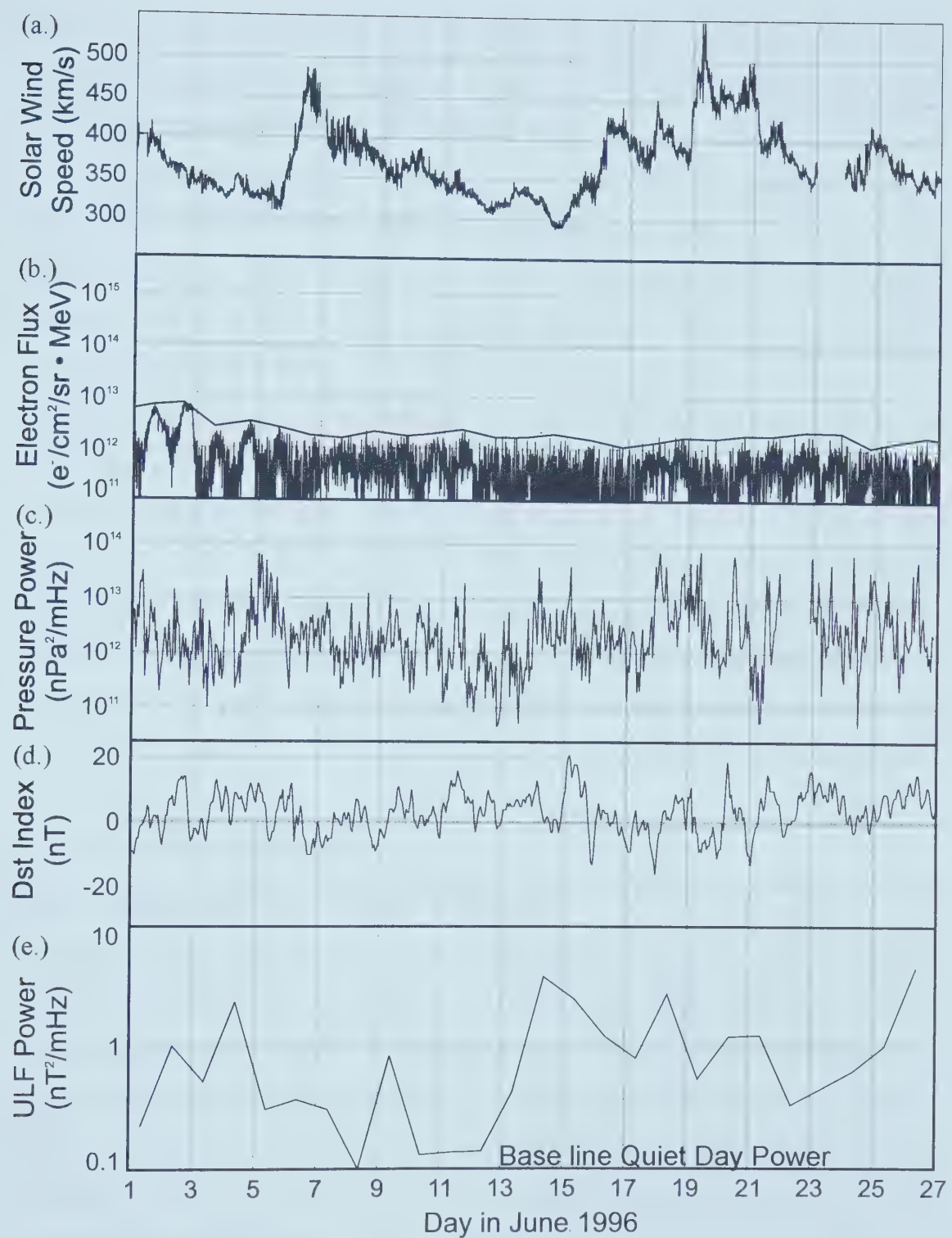


Figure 4.2 Space conditions from June 1 to 27, 1996. (a.) Solar wind speed; (b.) energetic ($E > 2$ MeV) electron flux measured by GOES 8; (c.) solar wind dynamic pressure power; (d.) Dst index and (e.) power in the ULF band calculated from ground based CANOPUS magnetometer data measured at Gillam, MB. The ULF power rises by more than one order of magnitude and yet the electron fluxes do not rise at all.

ground based magnetometer data in the ULF frequency band and electron energization, but it does indicate that another mechanism is needed to fully explain the enhanced fluxes of near-relativistic electrons near geostationary orbit.

4.1.3 No Pressure Power with Electron Enhancement

Figure 4.3 shows the only event which does not fit our model of increased pressure power associated with an electron energization event. The fluxes of energetic electrons, with no significant prior increase in solar wind pressure power, rise by almost two orders of magnitude beginning very late on February 11, 1996. Also at this time the power in the ULF frequency band is two orders of magnitude higher than the quiet day power. The solar wind speed climbs from about 400 km/s to a peak at just over 600 km/s. The energetic electron fluxes in this case may be enhanced due to the combination of several of the aforementioned possibilities. Since the solar wind speed is over 500 km/s and the power ground based magnetometer data in the ULF frequency band is high and the Dst index shows the presence of a storm, these effects, in combination may have caused the fluxes to rise as observed.

4.2 Other Considerations

4.2.1 Inward Drifting Electron Gradients

It may be thought that energetic electrons may be convecting and radially diffusing inwards and thereby increasing the fluxes of electrons with greater energy than 2 MeV near geostationary orbit. Figure 4.4 displays the electron fluxes near geostationary orbit as measured by GOES 8 during the February 1996 and May 1998 electron energization events. The fluxes are plotted for electrons with $E > 0.55$ MeV and for $E > 2$ MeV. These plots show that electrons over a wide energy range are being simultaneously energized near geostationary orbit. This issue has been dealt with in part by *Rostoker et al. [1998]* in showing that the increase in electron fluxes ($E > 400$ keV, which is the data threshold for the SAMPEX satellite which measured the data discussed by *Rostoker et al. [1998]*) can appear simultaneously over a broad range of L-shells between

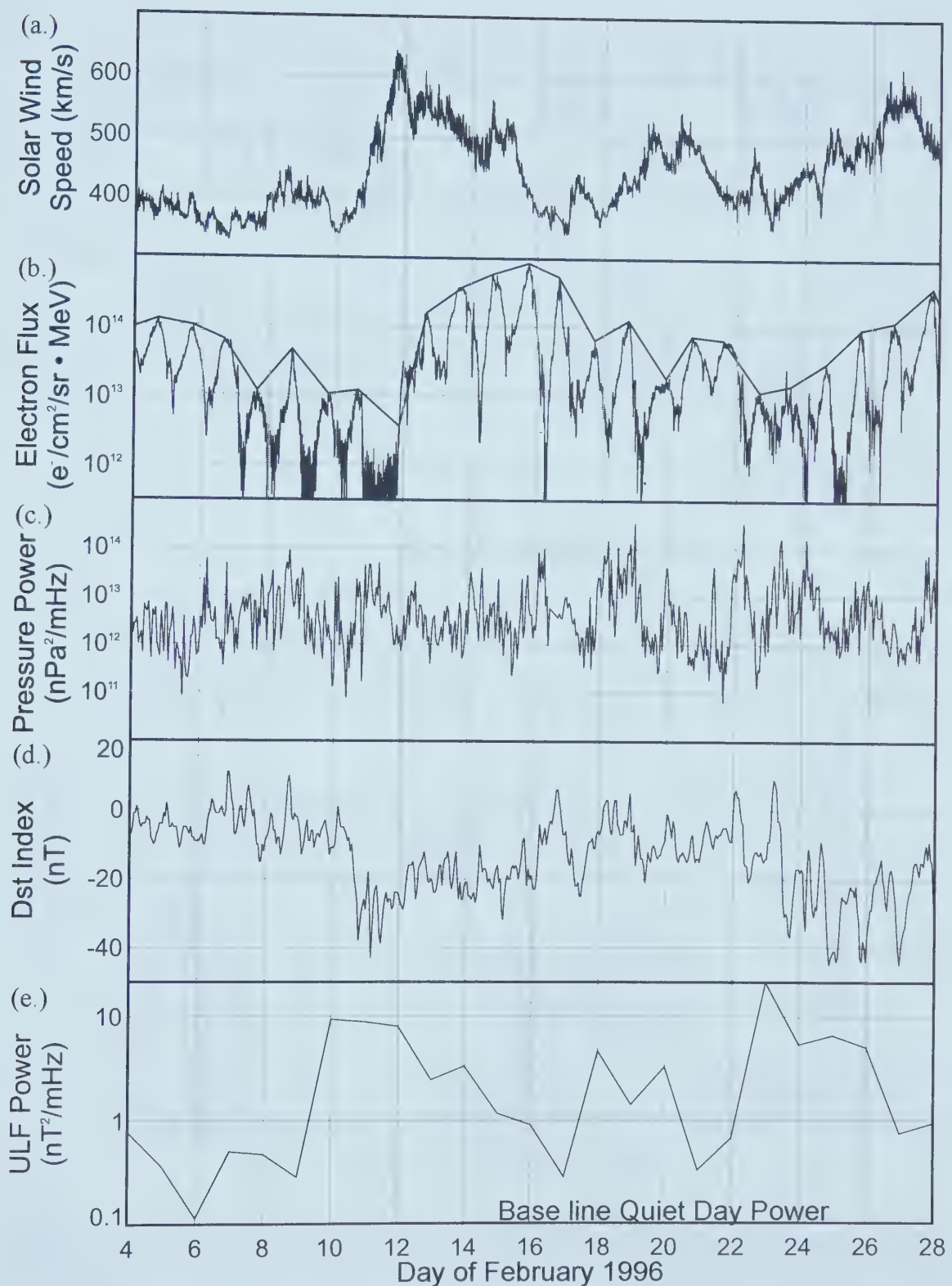


Figure 4.3 Space Conditions for February 1996. (a.) Solar wind speed; (b.) electron flux measured by GOES 8; (c.) solar wind dynamic pressure power; (d.) Dst index and (e.) the power in the ULF band of 2-20 mHz from 12:00-20:00 UT measured at Gillam, MB.

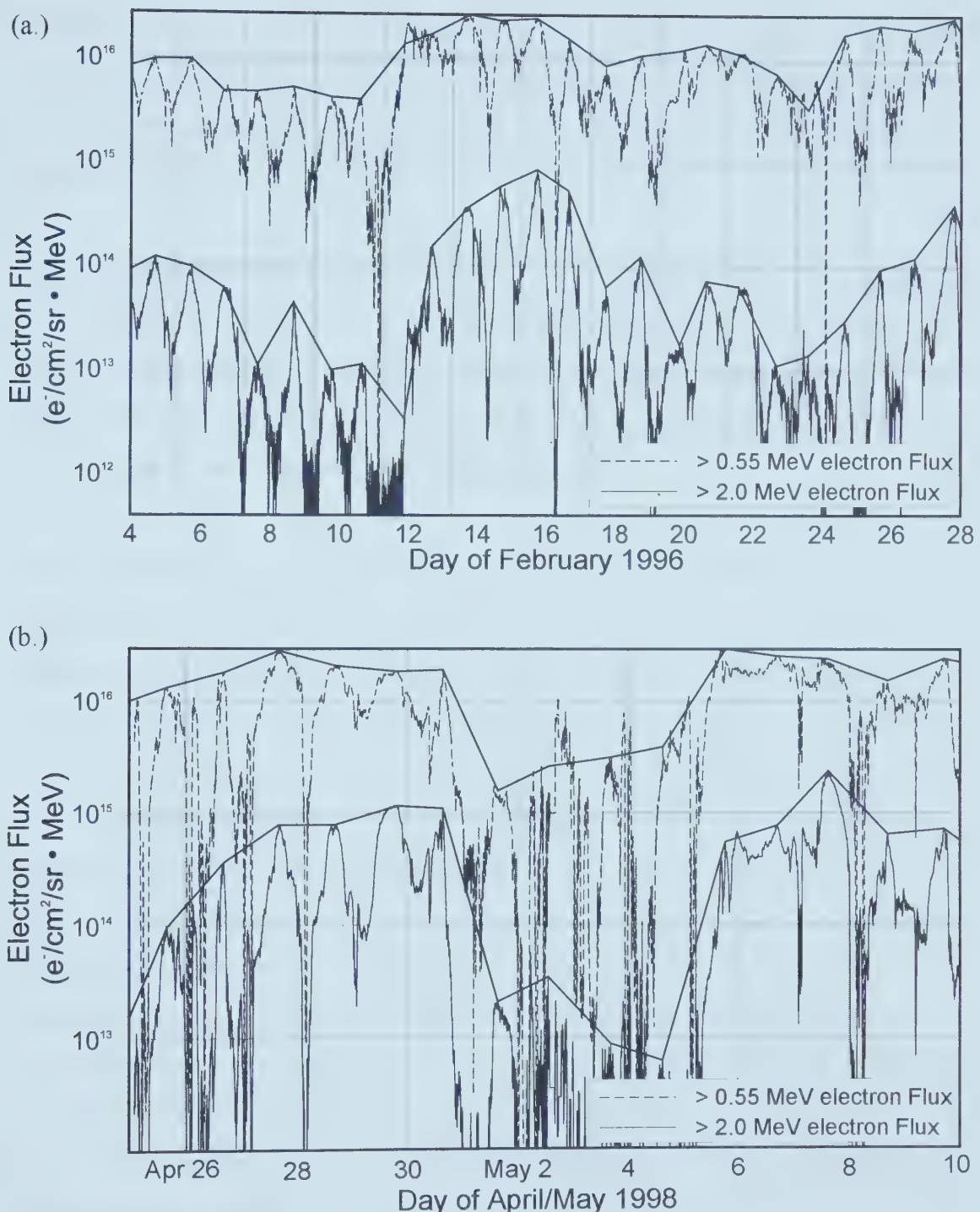


Figure 4.4 Electron fluxes measured by GOES 8 for (a.) February 1996 and (b.) April and May 1998. On both plots, the dashed curve is the electron fluxes with ($E > 0.55$ MeV) which is the lowest energy threshold of GOES 8 and the solid curve shows the fluxes of electrons ($E > 2.0$ MeV). The solid line on each curve connects the daily maximum values near local noon for GOES 8. The higher energy electron flux plots show the same shape as the lower energy flux plots.

the outer edge of the outer radiation belt and the magnetopause. They also write that there is no evidence that the electrons are transported inwards from the magnetotail, but that these energized electrons will over time, pass geostationary orbit as they radially diffuse earthward.

The above discussion establishes that electrons with $E > 400$ keV are not transported into the geostationary region. These electrons are rather energized after they arrive in the region near geostationary orbit. Yet the problem remains of whether or not electrons with $E < 400$ keV are transported into the geostationary region from the magnetotail and are energised to relativistic energies adiabatically.

4.2.2 High Energy Tail in the Electron Energy Spectrum

In the past, the possibility of plasma sheet electrons being the source population for near relativistic electrons detected at geostationary orbit had been discarded. This was on the basis of the low average energy of these electrons (about 2 keV at about $13.4 R_E$ behind the earth as seen in Figure 2.1) so that adiabatic acceleration could not possibly heat them to near-relativistic energies through inward transport to geostationary orbit. However, recently, T. Onsager (private communication) has considered the high energy tail of the plasma sheet electrons as a feasible seed population for the observed $E > 2$ MeV fluxes at geostationary orbit. He argues that the numbers of electrons in the high energy tail of a strongly heated plasma sheet might be significantly larger than for a normal active plasma sheet, providing a distribution as shown schematically in Figure 4.5. It might then be possible, with a 3 fold increase in energy, through conventional adiabatic acceleration during earthward transport, to achieve the observed fluxes of near-relativistic electrons near geostationary orbit. However, to date plasma sheet observations showing the required fluxes of high energy electrons in the tail have not been adequately investigated at times when relativistic electron events have been observed.

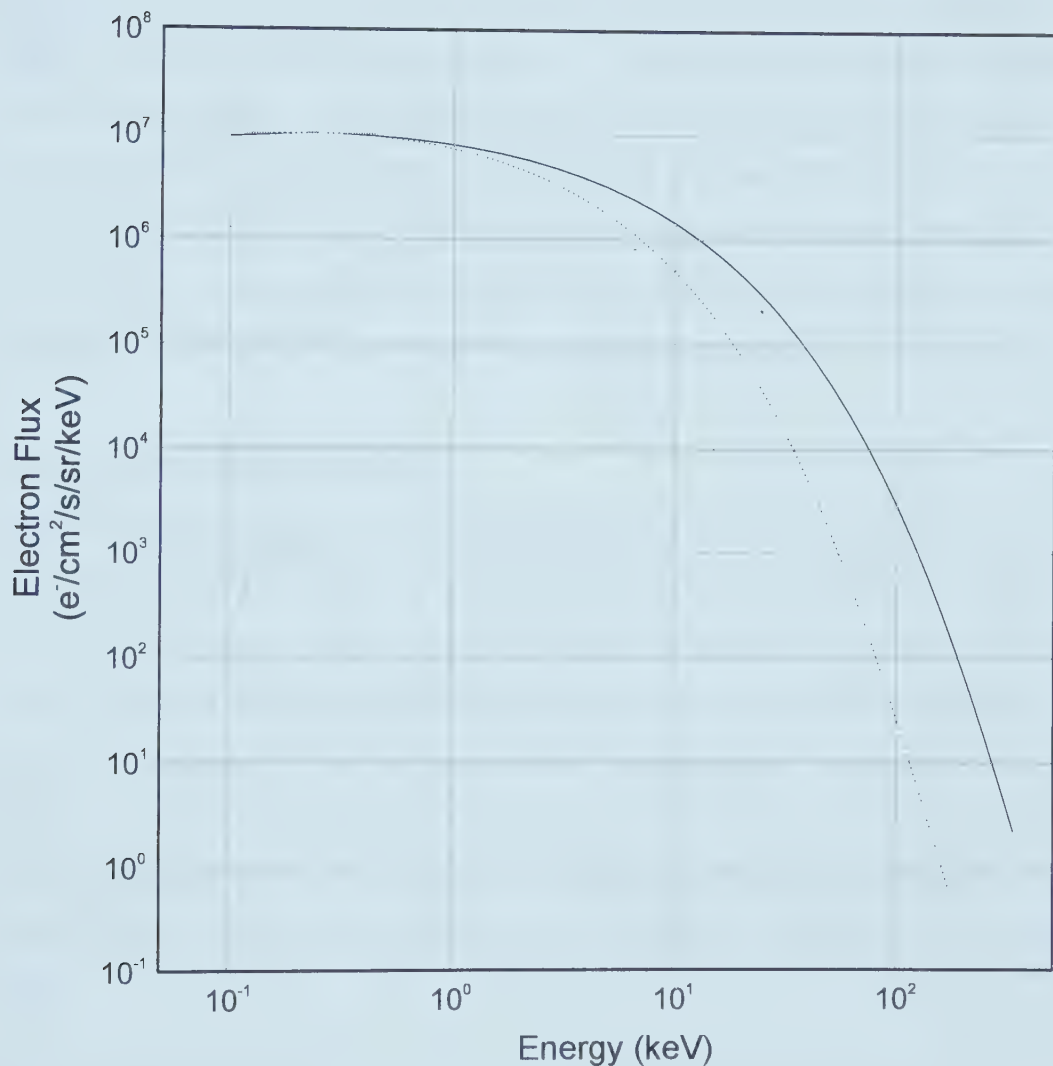


Figure 4.5 A schematic showing the high energy tail (no measured data) proposed by Onsager (solid curve) compared to the electron spectrum measured by the ISEE 1 satellite (dotted curve) also shown in Figure 2.1

4.2.3 Instrument Thresholding

The GOES energetic particle sensor provides information on the fluxes of electrons with $E > 2$ MeV and $E > 550$ keV. Energetic electrons with energies between 1 and 2 MeV would not be detected by the sensor whose threshold was 2 MeV, yet adiabatic acceleration due to some small earthward transport might provide enough energy to allow them to be detectable giving the appearance of a sudden episode of energization through a sharp rise in the $E > 2$ MeV electron fluxes. This would give a false impression of a population of lower energy electrons being accelerated to much higher energies in a very short period of time. While this is a possibility, if one uses the GOES data alone, it is unlikely that this unusual type of situation would lead to the large number of rises in near-relativistic electron fluxes detected at geostationary orbit.

4.3 Concluding Remarks

This study has investigated whether or not solar wind dynamic pressure power can play a role in energizing electrons near geostationary orbit to more than 2 MeV over a short time period. A positive answer does not eliminate other possible mechanisms but does provide a building block in solving the rapid energetic electron enhancement puzzle. This study was motivated by the fact that adiabatic acceleration of average energy central plasma sheet electrons does not provide enough energy to explain the observed fluxes near geostationary orbit. A secondary motivating factor is the practical ramifications of some satellites experiencing failure modes during times of elevated energetic electron fluxes.

Prior to this study *Rostoker et al.* [1998] have noted that the power in the ULF frequency band in the ground based magnetometer data rises just prior to a series of electron enhancements. This led us to investigate the source of the ULF electromagnetic waves. Two main sources of these ULF electromagnetic waves were briefly studied: KHI creating surface waves and global magnetospheric oscillations associated with solar wind pressure oscillations. Two models which incorporate global magnetospheric oscillations

into the electron energization process were discussed -- the toroidal pulsation model proposed by *Elkington et al.* [1999] and the compressional wave model proposed by *Liu et al.* [1999]. Initially in our investigation we noted that the solar wind was highly variable during many of the electron energization events. This caused us to more closely investigate this variation as a possible lead to a reason for the energization of electrons. The solar wind dynamic pressure power in the ULF frequency range, which is intimately related to the highly variable solar wind speed, was noted to be high just prior to enhancements of energetic electrons. We suggested that the solar wind dynamic pressure variations cause the global magnetospheric oscillations and drive the MHD waves in the compressional wave model proposed by *Liu et al.* [1999].

In studying 76 electron enhancements in the period of four years and displaying two sample events (one very high pressure power event on May 1998 and an average pressure power event on January 1995), we see that the solar wind dynamic pressure power in every case (except one) has risen prior to the electron enhancement. We note, as an important result, that every time during which the pressure power exceeded 10^{15} nPa²/mHz, an electron enhancement followed.

We also found that times with high pressure power just prior to an electron energization event are not always characterized by high speed solar winds. This is seen in the broad distribution of solar wind speeds for electron enhancements which are associated with high pressure power.

Thus for the fluxes of electrons to be enhanced near geostationary orbit, we find it necessary to have a significant power level ($> 10^{15}$ nPa² mHz) of solar wind dynamic pressure. When this pressure is lower than 10^{15} nPa² mHz, it seems that a combination of conditions are needed to enhance the fluxes of relativistic energies. Possible conditions include high solar wind speed, ground based ULF power and storm time DST values.

Although the answer to the question proposed by this thesis is positive (*i.e.* that increased solar wind pressure power may indeed be related to enhanced fluxes of relativistic electrons near geostationary orbit), this problem is far from being solved completely as is seen in our brief discussion of the counter examples. As with much of the work in space physics, more detailed measurements in more locations (*i.e.* more satellites with better instruments) would greatly enhance the likelihood of solving the puzzle surrounding the origin of the energetic electrons.

Some future work which needs to be done to further address the problem of the appearance of near-relativistic electrons near geostationary orbit includes how solar wind speed regulates the strength and occurrence of ULF magnetic pulsations detected by ground based magnetometers. If the KHI is the mechanism whereby the pulsations are generated, it remains to be seen how low solar wind speeds can be associated with enhanced near-relativistic electron fluxes. Additionally the energization of the plasma sheet in a way which affects the high energy tail of the distribution of energetic electrons (identified as an important component of a mechanism for producing near relativistic electrons at geostationary orbit by T. Onsager) requires further study. Clarifying these problems would go a long way to helping us understand why near-relativistic electrons appear in the vicinity of geostationary orbit from time to time.

Bibliography

Axford, W.I., H.E. Petschek, and G.L. Siscoe, Tail of the magnetosphere, *J. Geophys Res.*, **70**, 1231, 1965.

Baker, D.N., J.H. Allen, R.D. Belian, J.B. Blake, S.G. Kanekal, B. Klecker, R.P. Lepping, X. Li, R.A. Mewaldt, K. Ogilvie, T. Onsager, G.D. Reeves, G. Rostoker, R.B. Sheldon, H.J. Singer, H.E. Spence, and N. E. Turner, An assessment of space environmental conditions during the recent Anik E1 spacecraft operational failure, *ISTP Newslett.*, **6**, 8, 1996.

Baker, D.N., J.H. Allen, S.G. Kanekal, and G.D. Reeves, Disturbed space environment may have been related to pager satellite failure, *Eos Trans, AGU*, **79**, 477, 1998a.

Baker, D.N., J.B. Blake, L.B. Callis, R.D. Belian, and T.E. Cayton, Relativistic electrons near geostationary orbit: Evidence for internal magnetospheric acceleration, *Geophys. Res. Lett.*, **16**, 559, 1989.

Baker, D.N., J.B. Blake, R.W. Klebesadel, and P.R. Higbie, Highly relativistic electrons in the earth's outer magnetosphere, I, Lifetimes and temporal history 1979-1984, *J. Geophys Res.*, **91**, 4265, 1986.

Baker, D.N., and R. Carovillano, IASTP and solar-terrestrial physics, *Adv. Space Res.*, **20**, 531, 1997a.

Baker, D.N., S.G. Kanekal, J.B. Blake, B. Klecker, and G. Rostoker, Satellite anomalies linked to electron increases in the magnetosphere, *Eos Trans, AGU*, **75**, 401, 1994.

Baker, D.N., X. Li, J.B. Blake, and S. Kanekal, Strong electron acceleration in the Earth's magnetosphere, *Adv. Space Res.*, **21**, 609, 1998b.

Baker, D.N., X. Li, N. Turner, J.H. Allen, L.F. Bargatze, J.B. Blake, R.B. Sheldon, H.E. Spence, R.D. Belian, G.D. Reeves, S.G. Kanekal, B. Klecker, R.P. Lepping, K. Ogilvie, R.A. Mewaldt, T. Osanger, H.J. Singer, and G. Rostoker, Recurrent geomagnetic storms and relativistic electron enhancements in the outer magnetosphere: ISTP coordinated measurements, *J. Geophys Res.*, **102**, 14,141, 1997b.

Baker, D.N., and T.I. Pulkkinen, Solar disturbances and correlated geospace responses: Relativistic magnetospheric electron acceleration, in Proc. 31st ESLAB Symp., 'Correlated phenomena at the sun, in the heliosphere and in geospace', ESTEC, Noordwijk, The Netherlands, 199-206, 1997c.

Baker, D.N., T.I. Pulkkinen, X. Li, S.G. Kanekal, J.B. Blake, R.S. Selesnick, M.G. Henderson, G.D. Reeves, H.E. Spence, and G. Rostoker, Coronal mass ejections, magnetic clouds, and relativistic magnetospheric electron events: ISTP, *J. Geophys Res.*, **103**, 17,279, 1998c.

Baker, D.N., H.E. Spence, and J.B. Blake, ISTP: Relativistic particle acceleration and global energy transport, *Adv. Space Res.*, **20**, 1075, 1980.

Blake, J.B., D.N. Baker, N. Turner, K.W. Ogilvie, and R.P. Lepping, Correlation of changes in the outer-zone relativistic-electron populations with upstream solar wind and magnetic field measurements, *Geophys. Res. Lett.*, **24**, 927, 1997.

Biermann, L., Kometenschweife und solare Korpuskularstrahlung, *Z. Astrophys.*, **29**, 274, 1951.

Brice, N., Fundamentals of very low frequency emission generation mechanisms, *J. Geophys Res.* **69**, 4515, 1964.

Chan, A.A., Noncanonical Hamiltonian methods for particle motion in magnetospheric hydromagnetic waves, *J. Geophys. Res.*, **103**, 20501, 1998.

Chan, A.A., L. Chen, and R.B. White, Nonlinear interaction of energetic ring current protons with magnetospheric hydromagnetic waves, *Geophys. Res. Lett.*, **16**, 1133, 1989.

Chandrasekhar S., Hydrodynamic and Hydromagnetic Stability, Oxford University Press, London, Great Britain, 1961.

Chapman, S., and V.C.A. Ferraro, A new theory of magnetic storms, *Terrest. Magnet. Atmospheric. Electr.*, **36**, 77 and 171, 1931.

Chen, L., and A. Hasegawa, A theory of log-period magnetic pulsations 1. Steady state excitation of field-line resonance, *J. Geophys Res.*, **79**, 1024, 1974.

Christon, S.P., D.J. Williams, D.G. Mitchell, C.Y. Huang, and L.A. Frank, Spectral characteristics of plasma sheet ion and electron populations during disturbed geomagnetic conditions, *J. Geophys Res.*, **96**, 1, 1991. .

Coon, J.H., Vela Satellite Measurements of Particles in the Solar Wind and The Distant Geomagnetosphere, in *Radiation Trapped in the Earth's Magnetic Field, Proceedings of the Advanced Study Institute*, edited by B.M. McCormac, pp. 231-255, D. Reidel Publishing Company, Dordrecht, The Netherlands, 1966.

Cornwall, J.M., Scattering of energetic trapped electrons by very low frequency waves, *J. Geophys Res.*, **69**, 1251, 1964.

Dungey, J.W., Survey of Acceleration and Diffusion, in *Radiation Trapped in the Earth's Magnetic Field, Proceedings of the Advanced Study Institute*, edited by B.M. McCormac, pp. 389-397, D. Reidel Publishing Company, Dordrecht, The Netherlands, 1966.

Elkington, S.R., M.K. Hudson, and A.A. Chan, Acceleration of relativistic electrons via drift-resonant interaction with toroidal-mode Pc-5 ULF oscillations, *Geophys. Res. Lett.*, **26**, 3273, 1999.

Fairfield, D.H., Simultaneous measurements on three satellites and the observations of the geomagnetic tail at 1000 R_E , *J. Geophys Res.*, **73**, 6179, 1968.

Fälthammer, C.-G., Coefficients of Diffusion in the Outer Radiation Belt, in *Radiation Trapped in the Earth's Magnetic Field, Proceedings of the Advanced Study Institute*, edited by B.M. McCormac, pp. 398-402, D. Reidel Publishing Company, Dordrecht, The Netherlands, 1966.

Fujimoto, M., and A. Nishida, Monte Carlo simulation of energization of Jovian trapped electrons by recirculation, *J. Geophys Res.*, **95**, 3841, 1990a.

Fujimoto, M., and A. Nishida, Energization and anisotropization of energetic electrons in the Earth's radiation belt by the recirculation process, *J. Geophys Res.*, **95**, 4265, 1990b.

Fujita, S., K.H. Glassmeier, and K. Kamide, MHD waves generated by the Kelvin-Helmholtz instability in a nonuniform magnetosphere, *J. Geophys Res.*, **101**, 27,317, 1996.

Goertz, C.K., and R.A. Smith, The thermal catastrophe model of substorms, *J. Geophys Res.*, **94**, 6581, 1989.

Gupta, J.C., Some characteristics of large amplitude Pc5 pulsations, *Aust. J. Phys.*, **29**, 67, 1976.

Hamilton, D.C., G. Gloeckler, F.M. Ipavich, W. Stüdemann, B. Wilken, and G. Kremser, Ring current development during the great geomagnetic storm of February 1986, *J. Geophys. Res.*, **93**, 14,343, 1988.

Hines, C.O., The energization of plasma in the magnetosphere: Hydromagnetic and particle-drift approaches, *Planet. Space Sci.*, **10**, 239, 1963.

Isenberg, P.A., The Solar Wind, in *Geomagnetism (Volume 4)*, edited by J.A. Jacobs, pp. 1-69, Academic Press, San Diego, USA, 1991.

Jacobs, J. A., Y. Kato, S. Matsushita, and V.A. Troitskaya, Classification of geomagnetic micropulsations, *J. Geophys Res.*, **69**, 180, 1964.

Kennel, C.F., Consequences of a magnetospheric plasma, *Rev. Geophys.*, **7**, 379, 1969.

Kennel, C.F., and H.E. Petschek, Limit on stably trapped electron fluxes, *J. Geophys Res.*, **71**, 1, 1966.

Kim, H.-J., A.A. Chan, R.A. Wolf, J. Birn, Can substorms produce relativistic outer belt electrons? *J. Geophys. Res.* **105** 7721, 2000.

Kivelson, M.G., Physics of Space Plasmas, in *Introduction to Space Physics*, edited by M.G. Kivelson, and C.T. Russel, pp. 27-55, Cambridge University Press, New York, USA, 1995.

Lam, H., and G. Rostoker, The relationship of Pc5 micropulsation activity in the morning sector to the auroral westward electrojet, *Planet. Space Sci.*, **26**, 473-492, 1978.

Lanzerotti, L.J., and A. Wolfe, Particle Diffusion in the geomagnetosphere: Comparison of estimates from measurements of magnetic and electric field fluctuations, *J. Geophys Res.*, **85**, 2346, 1980.

Lengyel-Frey, D., R.A. Hess, R.J. MacDowall, R.G. Stone, N. Lin, A. Balogh, and R. Forsyth, Ulysses observations of whistler waves at interplanetary shocks and in the solar wind, *J. Geophys Res.*, **101**, 27,555, 1996.

Liu, W.W., and G. Rostoker, Energetic ring current particles generated by recurring substorm cycles, *J. Geophys Res.*, **100**, 21,897, 1995.

Liu, W.W., G. Rostoker, and D.N. Baker, Internal acceleration of relativistic electrons by large-amplitude ULF pulsations, *J. Geophys Res.*, **104**, 17,391, 1999.

Li, X., I. Roth, M. Temerin, J.R. Wygant, M.K. Hudson, and J.B. Blake, Simulation of the prompt energization and transport of radiation belt particles during the March 24, 1991 SSC, *Geophys. Res. Lett.*, **20**, 2423, 1993.

Lyons, L.R., R.M. Thorne, and C.F. Kennel, Pitch-angle diffusion of radiation belt electrons within the plasmasphere, *J. Geophys Res.*, **77**, 3455, 1972.

Lyons, L.R., and D.J. Williams, Quantitative Aspects of Magnetospheric Physics, D. Reidel Publishing Company, Dordrecht, The Netherlands, 1984.

McPherron, R.L., Physical Processes Producing Magnetospheric Substorms and Magnetic Storms, in *Geomagnetism (Volume 4)*, edited by J.A. Jacobs, pp. 593-739, Academic Press, San Diego, USA, 1991.

Musielak, Z.E., MHD waves and turbulence in the solar wind, in *Proceedings of the Third SOLTIP Symposium, Oct. 14-18, 1996*, Beijing, China, edited by X.S. Feng and M. Dryer, pp 339-344, International Academic Publishers, 1998.

NASA, GOES DataBook, Greenbelt, Maryland, USA (contract number NAS5-29500; GSFC Specification S-480-21A; Reference #S-415-19), 1996.

Nishida, A., Outward diffusion of energetic particles from the Jovian radiation belt, *J. Geophys Res.*, **81**, 1771, 1976.

Northrop, T.G., The Adiabatic Motion of Charged Particles, John Wiley & Sons, New York, USA, 1963.

Ogilvie, K.W., D.J. Chornay, R.J. Fritzenreiter, F. Hunsaker, J. Keller, J. Lobell, G. Miller, J.D. Scudder, E.C. Sittler, Jr., R.B. Torbert, D. Bodet, G. Needell, A.J. Lazarus, J.T. Steinberg, J.H. Tappan, A. Mavretic, E. Gergin, SWE, A comprehensive plasma instrument for the wind spacecraft, *Space Science Reviews* **71**, 55, 1995.

Parker, E.N., Dynamics of the interplanetary gas and magnetic fields, *Astrophys. J.*, **128**, 664, 1958.

Parks, G.K., Physics of Space Plasmas: An Introduction, Addison-Wesley Publishing Company, Redwood City, USA, 1991.

Paschmann, G., The Earth's Magnetosphere, in *Geomagnetism (Volume 4)*, edited by J.A. Jacobs, pp. 295-326, Academic Press, San Diego, USA, 1991.

Paulikas, G.A., and J.B. Blake, Modulation of trapped energetic electrons at $6.6 R_e$ by the direction of the interplanetary magnetic field, *Geophys. Res. Lett.*, **3**, 277, 1976.

Paulikas, G.A., and J.B. Blake, Effects of the Solar Wind on Magnetospheric Dynamics: Energetic Electrons at the Synchronous Orbit, in *Quantitative Modelling of Magnetospheric Processes*, edited by W.P. Olson, pp. 180-202, AGU, Washington, DC, USA, 1979.

Reeves, G.D., Relativistic electrons and magnetic storms: 1992-1995, *Geophys. Res. Lett.*, **25**, 1817, 1998.

Roberts, C.S., Electron Loss from the Van Allen Zones Due to Pitch Angle Scattering by Electromagnetic Disturbances, in *Radiation Trapped in the Earth's Magnetic Field, Proceedings of the Advanced Study Institute*, edited by B.M. McCormac, pp. 403-421, D. Reidel Publishing Company, Dordrecht, The Netherlands, 1966.

Roberts, C.S., Pitch-angle diffusion of electrons in the magnetosphere, *Rev. Geophys.*, **7**, 305, 1969.

Roederer, J.G., Dynamics of Geomagnetically Trapped Radiation, Springer-Verlag Berlin, Heidelberg, Germany, 1970.

Rostoker, G., S. Skone, and D.N. Baker, On the origin of relativistic electrons in the magnetosphere associated with some geomagnetic storms, *Geophys. Res. Lett.*, **25**, 3704, 1998.

Rostoker, G., and B.T. Sullivan, Polarization characteristics of Pc5 magnetic pulsations in the dusk hemisphere, *Planet. Space Sci.*, **35**, 429, 1987.

Russell, C.T. (ed.), The Global Geospace Mission, Kluwer Academic Publishers, Dordrecht, The Netherlands, 1995.

Russell, C.T., and R.L. McPherron, Semiannual variations of geomagnetic activity, *J. Geophys Res.*, **11**, 111, 1973.

Scarf, F.L., F.V. Coroniti, D.A. Gurnett, and W.S. Kurth, Pitch-angle diffusion by whistler mode waves near the Io plasma torus, *Geophys. Res. Lett.*, **6**, 653, 1979.

Sentman, D.D., and C.K. Goertz, Whistler mode noise in Jupiter's inner magnetosphere, *J. Geophys Res.*, **83**, 3151, 1978.

Sentman, D.D., J.A. Van Allen, and C.K. Goertz, Recirculation of energetic particles in Jupiter's magnetosphere, *Geophys. Res. Lett.*, **2**, 465, 1975.

Sentman, D.D., J.A. Van Allen, and C.K. Goertz, Correction to "Recirculation of energetic particles in Jupiter's magnetosphere", *Geophys. Res. Lett.*, **5**, 621, 1978.

Schulz, M., The magnetosphere, in *Geomagnetism (Volume 4)*, edited by J.A. Jacobs, pp. 87-281, Academic Press, San Diego, USA, 1991.

Speiser, T.W., The geomagnetic tail, in *Geomagnetism (Volume 4)*, edited by J.A. Jacobs, pp. 333-391, Academic Press, San Diego, USA, 1991.

Spjeldvik, W.N., and P.L. Rothwell, The earth's radiation belts, in *Handbook of Geophysics and the Space Environment*, edited by A.S. Jursa, Air Force Geophysics Laboratory, Air Force Systems Command, 1983.

Van Allen, J. A., G. H. Ludwig, E.C. Ray, and C.E. McIlwain, Observations of high intensity radiation by satellites 1958 Alpha and Gamma, *Jet Propul.*, **28**, 588, 1958.

Van Allen, J. A., and L.A. Frank, Radiation around the Earth to a radial distance of 107,400 km, *Nature*, **183**, 430, 1959.

Walt, M., *Introduction to Geomagnetically Trapped Radiation*, Cambridge University Press, 1994.

West, H.I., Jr., R.M. Buck, and G.T. Davidson, The dynamics of energetic electrons in the Earth's outer radiation belt during 1968 as observed by Lawrence Livermore National Laboratory's spectrometer on OGO 5, *J. Geophys Res.*, **86**, 2111, 1981.

Wolfe, A., L.J. Lanzerotti, and C.G. Maclennan, Dependence of hydromagnetic energy spectra of solar wind velocity and interplanetary magnetic field direction, *J. Geophys Res.*, **85**, 114, 1980.

Williams, D.J., E.C. Roelof, and D.G. Mitchell, Global magnetospheric imaging, *Rev. Geophys.*, **30**, 183, 1992.

Williams, D.J., D.G. Mitchell, C.Y. Huang, L.A. Frank, and C.T. Russell, Particle acceleration during substorm growth and onset, *Geophys. Res. Lett.*, **17**, 587, 1990.

Zelenyi, L., A. Galeev, and C.F. Kennel, Ion precipitation from the inner plasma sheet due to stochastic diffusion, *J. Geophys Res.*, **95**, 3871, 1990.

University of Alberta Library



0 1620 1217 9428

B45483